

UFR SCIENCES ET TECHNIQUES DE NANTES - IMT ATLANTIQUE

CHLOÉ THERREAU

Master 2, Recherche en Physique Subatomique

Calibration of the XENON1T experiment at low energy using a Kr83m Source



Supervisor : **Julien Masbou**
Subatech (Nantes)



Ce que nous savons est une goutte
d'eau ; ce que nous ignorons est
l'océan.

Isaac Newton

Remerciements

Je souhaite remercier l'ensemble des membres du Groupe Xénon qui m'ont accueilli et m'ont fait confiance pour réaliser ce stage à leurs côtés. Merci de m'avoir permis d'évoluer dans un environnement exceptionnel et surtout de découvrir cette expérience passionnante de physique actuelle : XENON1T.

Merci à Dominique Thers pour avoir rendu possible la réalisation de ce stage au sein du Groupe Xénon.

Bien évidemment, je remercie Julien Masbou, pour son accueil, sa présence, sa bonne humeur et surtout pour son aide et pour tout ce qu'il a pu m'apprendre.

Un merci particulier à Sara Diglo pour m'avoir transmis ses connaissances et pour avoir répondu à mes interrogations.

Merci également à tous les professeurs du Master ARS qui nous ont transmis leurs savoirs et m'ont donné envie de poursuivre vers de plus grandes aventures.

Je souhaite aussi remercier le personnel administratif et informatique du laboratoire, toujours prêt à répondre mes questions.

Merci à mes camarades (Manuel et Corentin) pour ces midis très plaisants !

Enfin, merci à E. pour ton soutien sans faille.

Contents

Remerciements	v
Introduction	1
1 Dark Matter	2
1.1 Evidences	2
1.2 Dark Matter Properties	2
1.3 Relevant WIMPs Properties in Direct Detection Search	3
2 The XENON1T experiment	5
2.1 Detector Design	5
2.2 Interaction in Liquid Xenon	6
2.2.1 Signal Production	6
2.2.2 Electronic Recoil and Nuclear Recoil Discrimination	7
2.3 Calibration in XENON1T	8
2.3.1 Principle	8
2.3.2 Position Reconstruction	8
2.3.3 Correction	9
2.3.4 Energy Reconstruction	9
2.4 Data Processing	10
3 ^{83m}Kr Characteristics and XENON1T monitoring	11
3.1 Calibration with a ^{83m}Kr source	11
3.1.1 ^{83m}Kr Characteristics	11
3.1.2 ^{83m}Kr signal in XENON1T	12
3.1.3 Events selection	14
3.2 Determination of Calibration Quantities	16
3.2.1 Light Yield	16
3.2.2 Charge Yield	18
3.2.3 Electron Lifetime	19
3.2.4 Energy Resolution	20
3.2.5 Conclusion	21
4 Study at different electric fields	22
4.1 Uncorrected Signals	22
4.2 Light Yields dependence with the electric field	22
4.3 Charge Yield and Electron Lifetime dependence with the electric field	23
4.4 Energy Resolution dependence with the electric field	23
4.5 Conclusion	24
Conclusion and Outlook	25
A Method used to compute the means values in slices	26

B Calibration Campaign of the February, 22th and 23th, 2017	28
C Evolution of Calibration quantities over time	31
D Determination of the Electrons' Velocities at Different Drift Fields	35
E Evolution of Calibration quantities with the drift field	37
Abstract	44

Introduction

In the last century, several astrophysical observations indicated that a large part of the Universe's mass is composed of an invisible form of matter. This "Dark Matter" represents approximately 26% of the Universe's energy, while ordinary matter (Stars, Planet) represents only 5% of the Universe¹.

The scientific community deploys considerable efforts to find Dark Matter.

In a particle physics approach, based on models beyond the Standard Model, Dark Matter may consist of Weakly Interactive Massive Particles (WIMPs). Among the different methods to detect WIMPs, direct detection experiment using liquid xenon have shown the highest sensitivities over the past years. XENON1T, the third detector of the XENON collaboration, is nowadays the most sensitive direct detection experiment to a spin-independent WIMP-nucleus interaction. XENON1T is a dual-phase time projection chamber filled with 2 000 kg of liquid xenon. The XENON collaboration regroups 135 scientist, from 23 institutions based in 10 different countries.

To detect Dark Matter particles, the detector response to an energy deposit has to be well-known, particularly at low-energy, where Dark Matter is expected to manifest. Besides, XENON1T has to record data during several years in order to maximize the probability of detecting a WIMP-nucleus scattering: its response has to be well-known on all the Dark Matter period search, and has to be as stable as possible.

Therefore, several calibration sources are used by the XENON collaboration. In this work, we will focus on the XENON1T calibration using a ^{83m}Kr source, which emits two radiations at low-energy.

In the first chapter, we will introduce several evidences that argue the existence of Dark Matter and will discuss the expected WIMP-nucleus interaction properties. Afterwards, we will present the XENON1T experiment and how it is designed to detect these interactions (Chapter 2).

The third chapter will give an overview of the ^{83m}Kr characteristics and will discuss in details our analysis. The aim of this work is to study the detector response at low energy by calculating the Light Yield, the Charge Yield, the Electron lifetime and the Energy Resolution of XENON1T, essential observables which will be introduced in Chapter 3. Finally, we will study the stability of these quantities over time (Chapter 3) and at different electric fields applied in the time projection chamber (Chapter 4).

¹The Dark Energy represents the remaining 69% of the Universe's energy.

1.1. Evidences

The concept of Dark Matter (DM) was introduced to explain several astrophysics observations which indicate the presence of a missing mass in the universe. This invisible matter (i.e. with no light emission in all the electromagnetic spectrum) interacts very weakly with baryonic matter and is actively sought by physicists.

First evidences of the existence of DM came from astrophysical observations on galaxies and on galaxy clusters. In 1933, Fritz Zwicky studied the Coma Cluster and calculated its total mass based on gravitational effects. The speeds of the galaxies in the Coma Cluster implied that this mass was **400 times bigger** than the mass estimated based on the cluster's light. Zwicky introduced a new concept of non-luminous matter to explain his observations: dark matter [1].

Then, in the late 1970's, Vera Rubin and W. Kent Ford Jr studied the rotational velocity of stars in spiral galaxies [2]. It is related to the centripetal force which compensates the gravitational force, and decrease as the square root of the distance between stars and the center of the galaxy. However, as shown in Figure 1.1, the rotational curves of spiral galaxies are roughly constant with the distance between the star and the center of the galaxy. The **gravitational force required for these velocities must come from a halo of massive matter** that surrounds each galaxy, and represents approximately 10% of its total mass [2].

In the following years, others observations (hot gases properties in galaxy clusters, gravitational lens, cluster collisions) lead to the same conclusion: there is a non-visible matter in the universe.

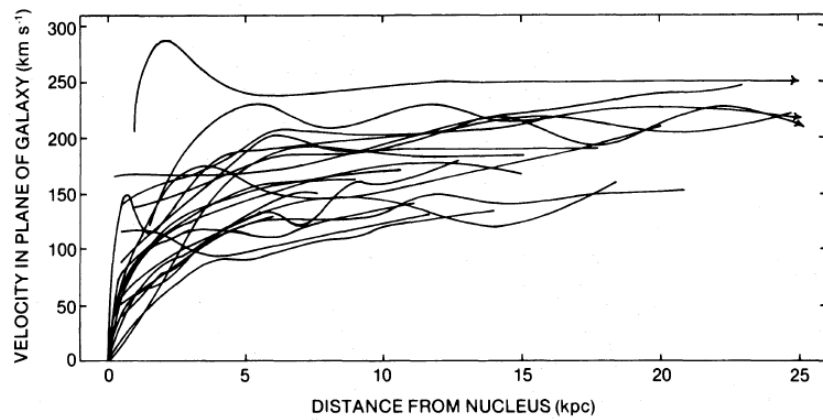


Figure 1.1 – Rotation curves for 21 spiral galaxies [2]. The rotational curves of spiral galaxies are roughly constant with the distance between the star and the center of the galaxy. The gravitational force required for these velocities must come from a halo of massive matter that surrounds each galaxy.

1.2. Dark Matter Properties

Even if DM is still unknown, some of its properties can be deduced from astrophysical observations.

First, by the difficulties to detect it, we can already deduce that DM is **non-radiative** and **neutral**¹. Secondly, by studying the early universe, an interaction cross-section of the order of the **weak** interaction has to be introduced to reproduce the relic abundance of DM [3].

Thirdly, from the observations on galaxies and on galaxy clusters mentioned in the previous section, we can infer that DM is present as a halo that surrounds all galaxies.

Fourthly, by studying the formation of large structures in the Universe, we can deduce that DM is **non-relativistic** ("cold") and present from the beginning of the Universe (i.e. **stable**). Indeed, to reproduce the distribution of large structure in the universe, a non-relativistic DM has to be introduced into the numerical simulations that attempt to recreate the evolution of the Universe as we know it today [4].

Finally, among others, the cosmic microwave background (CMB) contains information about the nature (**non-baryonic**) and the density of DM in the Universe. By measuring the CMB anisotropies, the Planck collaboration brought out that the DM density represents **26% of the Universe's density** [5].

Based on these properties, many candidates have been proposed for DM. In a particle physics approach, based on models beyond the Standard Model (SM), one of the best candidate is a class of massive particles which weakly interact with standard matter, called **Weakly Interactive Massive Particles (WIMPs)**. One of the extensions of the SM is the Minimal Supersymmetric Standard Model (MSSM) which predicts a supersymmetric partner for each SM particles. In particular, the MSSM predicts four neutralinos which the lightest of them is supposed to be stable and is an excellent candidate for DM [6].

1.3. Relevant WIMPs Properties in Direct Detection Search

Since our galaxy is supposed to be surrounded by a DM's halo, when the Sun (and thus the solar system) rotates around the center of the Milky Way, WIMPs should pass through the Earth and could interact with it. DM direct detection's working principle is based on the proposal of M. Goodman and E. Witten [7]. In 1985, they extended the neutral current neutrino detection to the DM detection: WIMPs are expected to interact with a nucleus through **elastic scattering**, during which the WIMP will transfer a part of its energy through a nuclear recoil, as shown in Figure 1.2.

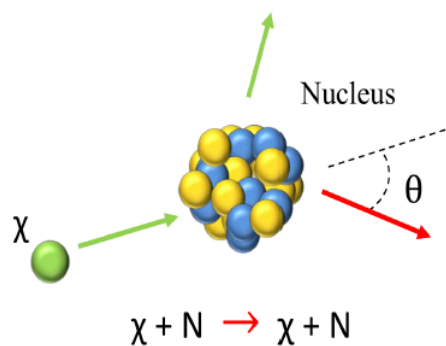


Figure 1.2 – Drawing of a WIMP-nucleus elastic scattering [3]. χ represents a WIMP, N a nucleus and θ the scattering angle.

The nuclear recoil energy expected in direct detection can be computed, by applying the conservation of energy and momentum:

$$E_{nr} = \frac{m_\chi v^2}{2} \frac{4m_\chi m_N}{(m_\chi + m_N)^2} \cos^2 \theta \quad (1.1)$$

Where m_χ and v are the mass and the relative velocity of the WIMP, m_N is the nucleus mass and θ is the scattering angle. At the scale of our galaxy, the WIMP's relative velocity distribution follow a

¹Charged particles will interact with standard matter through the electromagnetic force.

maxwellian function with a average value of $v \approx 230$ km/s. This value equals to the solar system velocity around the galactic center [8]².

The WIMP mass is expected between $10 \text{ GeV}/c^2$ and $10 \text{ TeV}/c^2$ [9]. For a direct detection experiment using, for example, xenon atom as target ($m_N \approx 131.29 \text{ u}$) (and with $\theta = 0$), the nuclear recoil energy transferred by a WIMP with a mass of $35 \text{ GeV}/c^2$ is: $E_{\text{NR}} \approx 10 \text{ keV}$.

We will keep in mind that a WIMP-nucleus scattering may induce an energy transfer from **a few keV to 100 keV**.

Finally, in May 2017, the XENON collaboration published the best world DM sensitivity limits. This limits was obtained by the XENON1T experiment on only **34.2 days** [10]. Figure 1.3 presents the 90% confidence level on the spin-independent WIMP-nucleon cross-section and shows a minimal cross-section of $7.7 \cdot 10^{-47} \text{ cm}^2$ for a WIMP mass of $35 \text{ GeV}/c^2$. This results improve by **a factor 15** the sensitivity of the 477 live days of XENON100, the previous experiment of the XENON collaboration [11].

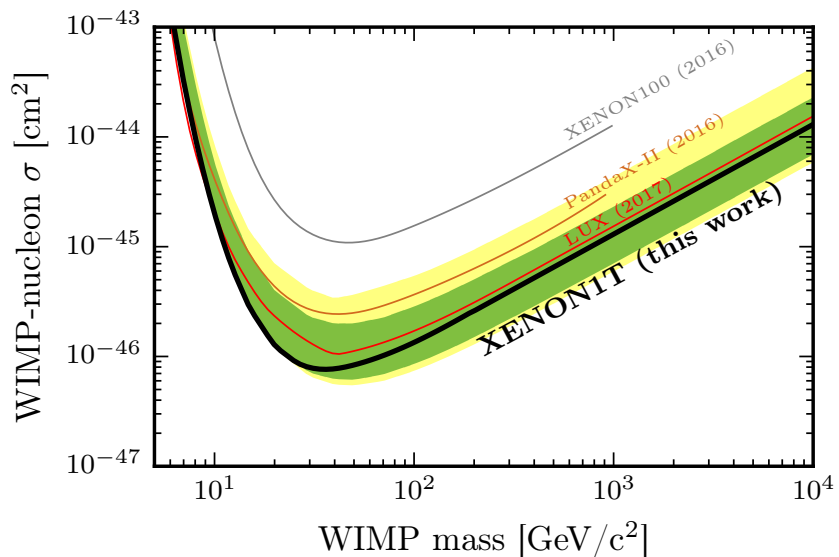


Figure 1.3 – XENON1T upper limits of the spin-independent elastic WIMP-nucleon cross section as a function of the WIMP mass at 90% C.L. Results of LUX, PandaX and XENON100 (i.e. more recent DM direct detection experiments using xenon) are shown for comparison [10].

²To take into account the possible escape of WIMPs from the gravitational attraction of the galaxy, a maximum speed is imposed ($v_{\text{max}} = 650 \text{ km/s}$).

The XENON1T experiment

XENON1T is located at the Laboratori Nazionali del Gran Sasso (LNGS) in Italy. It is a dual-phase (gas-liquid) Time Projection Chamber (TPC) filled with xenon (Xe), designed to detect the low-energy and rare scattering of WIMPs with Xe nuclei. The TPC and its two arrays of photomultiplier tubes (PMT) allow the detection of the light and charge signals produced by a particle interaction with Xe atoms. The TPC allows the determination of the 3D position of the interaction and the discrimination of the incoming particle (see section 2.3 and 2.2).

2.1. Detector Design

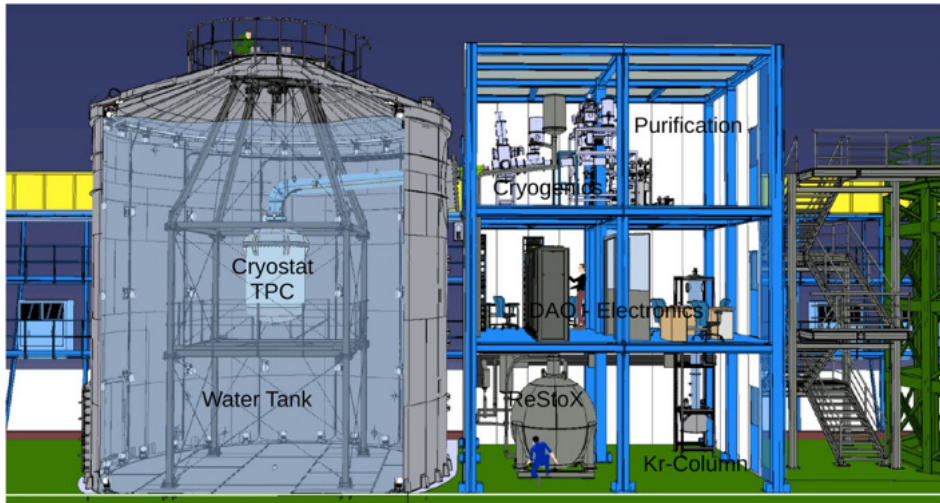


Figure 2.1 – View of the XENON1T detector. The LXe detector (TPC) and the inner-shielding are placed inside a cryostat. The water tank is used as an outer-shielding and as a muon veto detector. ReStox is a Xe emergency recovery system. A distillation column is added to the purification system to filter the ^{85}Kr , naturally present in xenon [12].

Liquid Xenon (LXe) was chosen as detector medium for different reasons.

First, LXe is an **efficient scintillator**, transparent to its own scintillation, allowing the detection of scintillation signals.

Secondly, since WIMP-nucleus interaction is expected to be a rare event (as shown in Chapter 1), the interaction probability has to be maximized: Xe nucleus has a **high atomic number** ($A=131$) which provides a high event rate since the interaction cross section between WIMP and standard matter is proportional to A^2 [13]. Besides, LXe has a **high density** ($\rho_{\text{LXe}} = 2.953 \text{ g/cm}^3$, at 177 K [13]) which allows the probability of WIMP scattering to be increased.

Thirdly, the background event rate has to be minimized: LXe has the interesting property of having low **intrinsic radioactivity**. LXe has a **high stopping power**, providing a self-shielding from ambient radioactivity (another 1 200 kg of LXe is added and provides a inner-shielding [10]). Besides, XENON1T is placed at an depth of 3 600 m equivalent water under the Gran Sasso mountain, reducing the background noise coming from cosmic ray. The TPC is also placed inside a ultra pure

water tank, used as a outer-shielding and as a muon veto detector (by detecting the Cherenkov light emitting by cosmic muons that interact with water).

Finally, contaminants are naturally present in LXe. A recirculation purification system is continuously used to reduced the intrinsic contaminant concentration, such as electronegative impurities (that could attenuate the charge and light signals, see section 2.3.3).

2.2. Interaction in Liquid Xenon

2.2.1. Signal Production

In LXe, we distinguish **two types of interactions** depending on the projectile. If the incoming particle is a WIMP or a neutron (with an energy around a few MeV), an elastic scattering with a nucleus will lead to a **Nuclear Recoil** (NR), as shown in section 1.3. If the incoming particle is a photon (with a typical energy of [0.1, 10] MeV, since it will come from the ambient radioactivity), a photoelectric effect, a Compton Effect or a electron-positron pair creation will lead to an **Electronic Recoil** (ER). In the same way, ER can be induced by β particles (i.e. electrons) which interact with atomic electrons through elastic scattering [14].

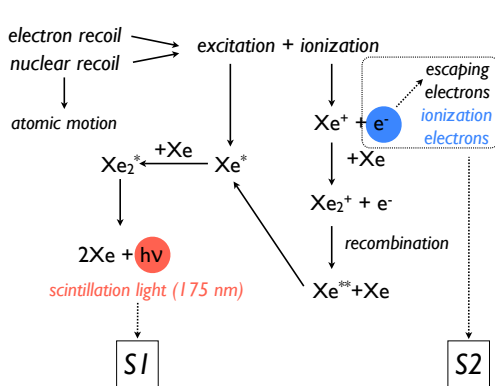


Figure 2.2 – Illustration of the signals production in the XENON1T TPC [3].

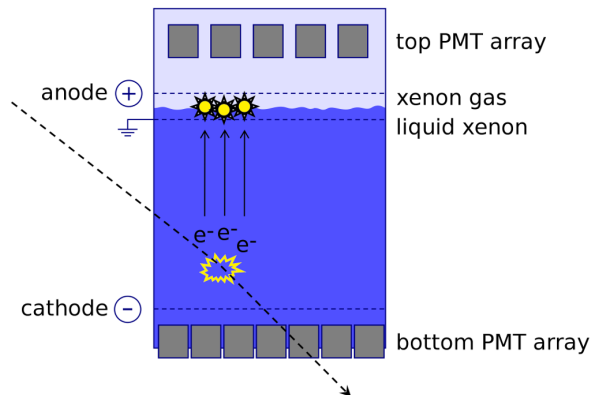


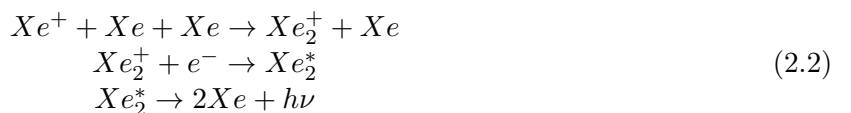
Figure 2.3 – Working principle of the XENON1T TPC, showing the S1 and S2 signals production. The black arrow shows an incoming particle [15]

In both case, Xe atoms are ionized and excited. Two signals are produced: a **light signal, S1** and a **"charge" signal, S2**, as shown in Figure 2.2

As indicated in equation 2.1, the light signal is produced when the excited Xe atoms form with another Xe atom an excited state. The excited dimer Xe_2^* decays to the ground state after a few ns, emitting the first scintillation signal (S1). Scintillation in LXe has a typical wavelength of 178 nm.



Ionized atoms are also involved into the light signal production, as shown in equation 2.2 and summarized in Figure 2.2. Indeed, an ionized atom can recombine with free electrons (i.e. electrons that come from the ionization) and form an excited dimer of Xe_2^* . The excited Xe_2^* decays to the ground state by emitting scintillation light (i.e. S1 signal).



As shown in Figures 2.2 and 2.3, the charge signal (i.e. S2 signal) is produced by the electrons coming from the ionization of Xe atoms. If an electric field (called the drift field) is applied on the TPC, these electrons can escape the recombination with Xe atoms. The drift field guides the electrons to the gas phase (GXe) at the top of the TPC. There, an other electric field extracts the

electrons from the liquid phase to the gas one. During the extraction, the proportional scintillation signal, S₂, is produced¹. In XENON1T, the drift field has a nominal strength of 120 V/cm; the extraction field has a strength of 13 kV/cm [10].

Ionization participate to both signals. As a consequence, **S1 and S₂ are anti-correlated**. As shown in Figure 2.4, the higher the drift field is, the more electrons can escape the recombination, giving a larger S₂, but, a smaller S₁² (this behaviour will be verified in Chapter 4).

The proportion of charge and light signal is different at different fields but their sum is constant, giving the possibility of improving the Energy Resolution by combining the two signals. This will be investigated in section 3.2.4.

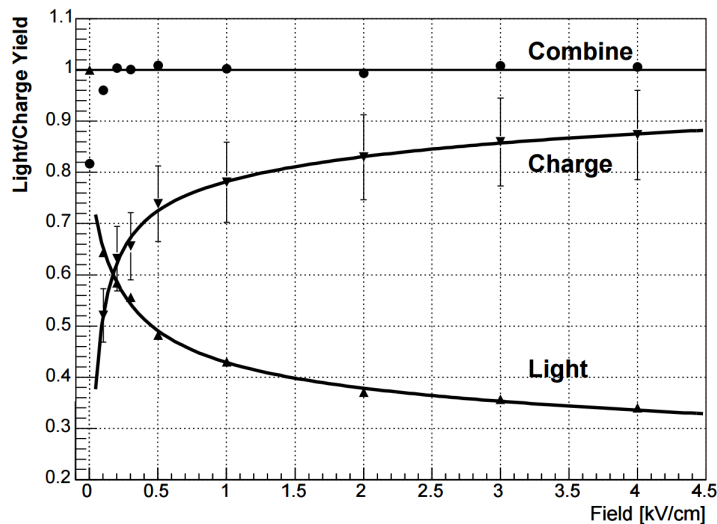


Figure 2.4 – Light and Charge Yields as a function of drift field for 662 keV gamma-rays from ^{137}Cs . The light and charge signals are anti-correlated: when the drift field increases, the Charge Yield increases, while the Light Yield decreases [16].

The light and charge signals produced in the TPC allow the reconstruction of **3D position** of the interaction as well as the **discrimination of the incoming particle** (see section 2.3).

The TPC is a cylinder of 95.8 cm wide by 96.9 cm long that encloses 2 000 kg of xenon. Two PMTs³ arrays, one at the top and one at the bottom of the TPC, allow the detection of S₁ and S₂ signals, as shown in Figure 2.3 [10].

2.2.2. Electronic Recoil and Nuclear Recoil Discrimination

Electronic Recoil and Nuclear Recoil can be distinguished thanks to the relative intensity of S₁ and S₂ signals, i.e. the **S₂/S₁ ratio**. Indeed, in LXe, NR have a higher ionization density than ER. Ionization density is the number of ions per unit of path length produced by a particle along its track. A higher ionization density leads to more ions and electrons in a smaller space, thus the recombination yield will be higher, giving a larger S₁ and smaller S₂ (since less electrons will escape from the recombination)

As a consequence, the **S₂/S₁ ratio will be lower for NR than for ER**, allowing a discrimination between these two types of recoil, and then, a discrimination between WIMP (or neutron) and electronic background (γ or β particles) [3].

¹The S₂ signal is called the Charge signal because it is produced thanks to electrons, but, in fact, it is a light signal.

²since electrons that do NOT escape the recombination participate to the S₁ signal production.

³A total of 248 PMTs is used

2.3. Calibration in XENON1T

Thanks to both S1 signals S2 signals and to calibration of the XENON1T detector, information about the interaction can be reconstructed.

2.3.1. Principle

Calibration is essential to study and understand the detector response. In the case of direct DM search, expected signals are induced by low-energy deposits, requiring a specific calibration from a few keV to 100 keV. To calibrate XENON1T, several sources with well-known energy deposits are employed [10].

For low-energy ER, calibration sources are usually γ emitters. Two "internal" sources are used: ^{220}Rn and ^{83m}Kr sources. Both are injected within LXe (as gas in the recirculation gas system, after the purification system) giving a homogeneous and spatially uniform deposit. ^{83m}Kr is also used to determine the spatial response of the detector [10].

^{220}Rn and its daughter isotopes emit several radiations, as shown in Figure 2.5, giving several range of applications [10]. ^{83m}Kr decays by two subsequent emissions of γ rays at 32.2 keV and 9.4 keV and will be study in detail in Chapter 3.

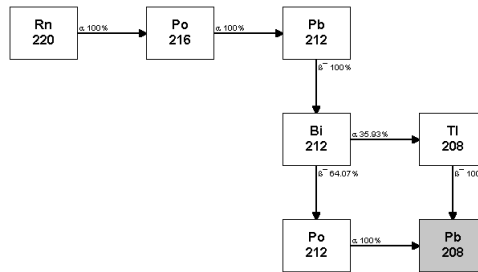


Figure 2.5 – ^{220}Rn decays [17]

For low-energy NR, calibration source are neutrons emitters. An external source of AmBe is placed at the edge of the cryostat into a tungsten collimator [18]. AmBe (chemical mixing of ^{241}Am and ^9Be) decays emitting neutrons, allowing a calibration to single scatter NR as shown in equation 2.3. AmBe source is also used for ER calibration thanks to the activation of ^{129}Xe , ^{131}Xe , ^{129m}Xe and ^{131m}Xe isotopes, naturally present in LXe and which decay emitting γ -rays [19].



2.3.2. Position Reconstruction

Since the S2 signal is produced close to the top PMT array, and since the electron travel is straight inside the TPC, the position of the S2 signal in the top PMT array gives the $x - y$ position, with a resolution below a few cm. The Z coordinate is determined thanks to the electron drift inside the TPC. It has a resolution of the order of 100 μm .

Z coordinate is proportional to the Drift Time (Δt), which is equal to the travel time of electrons and is determined by the time difference between the detection of S2 signal and S1 signal.

$$Z = v_d \cdot \Delta t \tag{2.4}$$

Where v_d is the electron drift velocity in LXe. It depends on the drift field applied in the TPC and on the electron mobility μ in LXe ($\mu \approx 2\,000 \text{ cm}^2 \text{ V}^{-1} \text{ s}^{-1}$ [20]).

The determination of the interaction position allows the selection of a fiducial volume at the center of the TPC, used to reduce the ambient radioactivity, mostly present at the edge of the detector.

2.3.3. Correction

It is important to note that, for a given energy, the amount of collected light and charge signals depends on the position interactions (because of solid angle effect, reflection of the TPC wall, PMT's efficiency etc...). To correct S1 and S2 signal depending on the interaction position, calibration sources (in particular ^{83m}Kr source), with well-known energy deposit, are used. The correction is expressed as the relative difference between measured signals and the expected energy deposit, depending on the interaction position, and are implemented in the Light Collection Efficiency Map (LCE map)[3].

For S2 signals, in addition of the $x - y$ position correction, the attenuation of the electrons cloud has to be considered. Indeed, because of electronegative impurities into the LXe, some of the electrons coming from the ionization are trapped during their drifts. As a consequence, the amount of S2 signals decreases exponentially with the Drift Time⁴. The evolution of the S2 signal as a function of the Drift Time can be written as in equation 2.5 [19].

$$S2 = S2_0 \cdot \exp\left(\frac{-\Delta t}{\tau}\right) \quad (2.5)$$

Where S2 is the charge signal that is measured after the electrons' drift, while $S2_0$ is the charge signal that should have been seen if no impurities were present in the LXe (i.e. at the top of the TPC). τ is the Electron Lifetime, that means the amount of time that half of the free electrons can remain in the detector before being swallowed up by an impurity. Therefore, it allows the measurement of the number of impurities inside the LXe and the correction of the S2 signals. It will be determined with the ^{83m}Kr source in section 3.2.3.

2.3.4. Energy Reconstruction

In addition of the interaction position, the energy transferred to the LXe can be reconstructed. The aim of such reconstruction is to convert signals (i.e. S1 and S2 signals, expressed in Photo-Electron (PE), the unit of PMT signals) into energy deposits (expressed in keV). Calibration sources are used to determine these conversion factors, that depend on the detector used and on the type of recoil studied.

For ER, the conversion factor between S1 (S2) signals and energies are called the Light (Charge) Yield as shown in equation 2.6 [3].

$$E_{ER} = \frac{S1}{Ly} \quad \text{and} \quad E_{ER} = \frac{S2}{Cy} \quad (2.6)$$

Where Ly is the Light Yield, Cy is the Charge Yield and E_{ER} is the transferred energy during an ER.

For NR, calibration sources are neutron emitters, which are not mono-energetic. As a consequence, the energy of the incomming neutron is not precisely known. To determine the energy transferred during a NR, S1 signal is rescaled as a ER signal. Therefore, the transferred energy during a NR, E_{NR} , is given in equation 2.7 [3].

$$E_{NR} = \frac{S1}{Ly} \frac{1}{\mathcal{L}_{\text{eff}}} \frac{S_e}{S_n} \quad (2.7)$$

Where Ly is the light yield for ER, \mathcal{L}_{eff} is the attenuation factor that accounts the conversion from NR to ER. \mathcal{L}_{eff} is the relative light yield of a NR energy compared to the light yield of the ER induce by the 122 keV γ ray of the ^{57}Co , when no field is applied into the TPC. S_e and S_n are introduced to take account of the attenuation of S1 signal (for ER and NR, respectively) due to the application of an electric field into the TPC [3] (see section 2.2).

⁴The deeper the interaction is, the more likely the electrons are trapped.

2.4. Data Processing

For XENON1T, a raw data processor called PAX (Processor for Analyzing XENON) was developed. PAX is a pure-python program and works as follow :

When a PMT detects a photon, a pulse can be observed. PAX finds the pulse, computes it and classifies it in peak: S1 peaks or S2 peaks, depending on its time width. S1 signals have a time width of a few ns, while S2 signals have a time width of a few μ s, since they are emitted along the path of the electrons in the gas gap between the liquid surface and the anode (as shown in Figure 2.3).

Here, PAX creates a ROOT file containing the processed data.

The classification is done late in the processing so it can use as much information about each peak as possible. Besides, if the classification and clustering algorithms are updated, a quick partial reprocessing suffices to propagate the update to all previously taken data [21]. Afterwards, HAX (Handy Analysis tools for XENON) extracts data from the ROOT file (thanks to "TreeMaker") and makes small ones (called "MiniTree") which contain the information needed for the analysis. For example, the "Basics" MiniTree will contain the number of event, the position interactions, the values of S1 and S2 signals etc...

On the rest of this report, we will used a ^{83m}Kr source, that decays by two subsequent radiations (see Chapter 3). Therefore, the MiniTree (i.e. ROOT files) exploited will contain information about double scatter events, that means, event with two S1 and two S2 signals.



Figure 2.6 – Pax Logo

^{83m}Kr Characteristics and XENON1T monitoring

As we perceive in the previous Chapter, calibration is vital to exploit the XENON1T response to an energy deposit, but also to study its stability. Indeed, XENON1T has to record data during several years in order to maximize the probability of detecting a WIMP-nucleus scattering: its response has to be well-known on all the DM period search, and has to be as stable as possible.

In the rest of this report, ^{83m}Kr will be used as a low-energy calibration source (i.e. in the energy range of interest for direct DM search), and will allow the determination of several essentials calibration quantities: **the Light Yield, the Charge Yield, the Electron Lifetime and the Energy Resolution** of the detector. Then, a off-line monitoring (using a semi-automatic algorithm) will be used to study the stability of these quantities during several months.

3.1. Calibration with a ^{83m}Kr source

In this section, we will present an overview of the ^{83m}Kr decays and of the signals we will obtain with XENON1T. We will then propose several cuts that allow the selection of ^{83m}Kr events with two S1 signals (one at 32.2 keV and the other at 9.4 keV), and one S2 signals (at 41.6 keV)¹.

3.1.1. ^{83m}Kr Characteristics

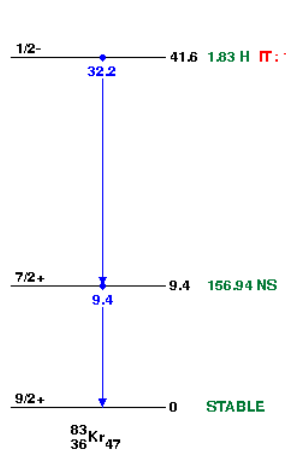


Figure 3.1 – ^{83m}Kr decay scheme [22]

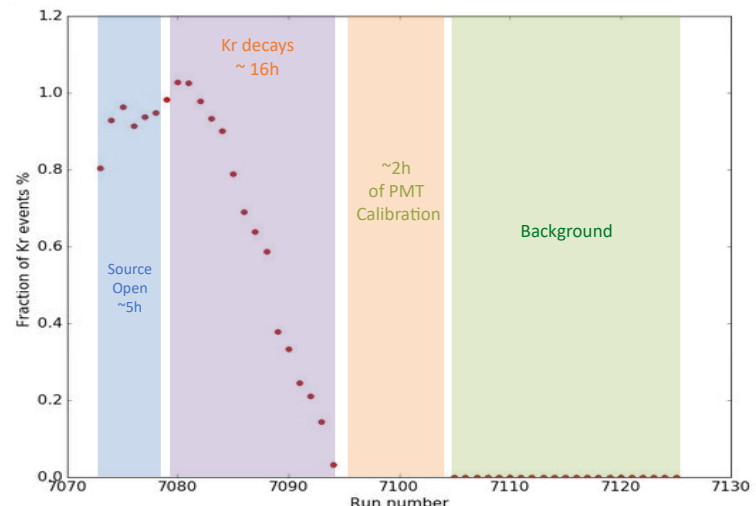


Figure 3.2 – Study of the ^{83m}Kr decay in XENON1T. Each run correspond to ≈ 1 hour.

To diffuse the ^{83m}Kr in the XENON1T TPC, a parent source of ^{83}Rb is used. A ^{83}Rb emanation chamber is placed on the purification system where the GXe passes through and entrains the ^{83m}Kr

¹Actually, there will always be two S1 and two S2, but the second S2 will not be used.

coming from the ^{83}Rb decay. ^{83m}Kr is **uniformly distributed** in the LXe, allowing the selection of a fiducial volume, at the center of the TPC, free of contamination from ambient radioactivity. ^{83m}Kr has an adapted half live of 1.83h: after a few hour, the radioactive components of ^{83m}Kr have disappeared form the detector, as shown in Figure 3.2. **This Figure was obtain by applying the event selections present in section 3.1.3, at the beginning of my work for the XENON collaboration**². A check was needed and shows that 24 hours after closing the source (open during 5 hours), DM data are not contaminated by ^{83m}Kr .

^{83m}Kr decays by **two subsequent emissions of γ rays at 32.2 keV and 9.4 keV**, as shown in Figure 3.1, allowing the study of the detector medium response in the region of interest for DM search. The two γ rays are spaced by an short average time of **156.94 ns** [22], allowing the **identification** of the ^{83m}Kr decay. At more than 10 times this values, it is very unlikely that two signals are produced by the decay of (the same) ^{83m}Kr atom.

3.1.2. ^{83m}Kr signal in XENON1T

In order to calibrate XENON1T, the energy deposit has to be well-known: we have to select events with two well-separated signals (one at 32.2 keV and the other at 9.4 keV).

S2 signals are emitted along the path of the electrons in the gas gap (between the liquid surface and the anode (as shown in Figure 2.3)), its time width is of the order of μs , bigger than the delay time (157 ns) between the two ^{83m}Kr radiations. As a consequence, **most of the two S2 signals are not separated during the reconstruction** of a ^{83m}Kr event, and are reconstructed as "pileup" events, with an energy of **41.6 keV** (32.2 keV + 9.4 keV). For S1 signals, pileup can also occurs when the time difference between the two S1 signals is small.

The short live-time of the 9.4 keV-level gives **different types of populations in XENON1T**, shown in Table 3.1.

Since S2 signals are not separated, the populations with two S2 signals have a very low-statistic and will not be used³. The population with **one S1 and one S2** (with the same energy of 41.6 keV) allows combination of S1 and S2 signals (used to improve the Energy Resolution, see sections 2.3 and 3.2.4). The population with **two S1 and one S2** is used to study the detector response at 32.2 keV and 9.4 keV (with S1) and at 41.6 keV (with S2).

Number of signals	1 S2 (41.6 keV)	2 S2 (32.2/9.4 keV)
1 S1 (41.6 keV)	Energy Resolution	Low-statistic
2 S1 (32.2/9.4 keV)	Ly, Cy, τ	Low-statistic

Table 3.1 – Overview of the different populations of a ^{83m}Kr decay in XENON1T. The text in red indicate on what kind of study the population will be apply. **Ly** means Light Yield, **Cy** means Charge Yield and τ is the Electron Lifetime.

The first step to select events with two S1 signals is to use the "DoubleScatter" TreeMaker, which was coded by a researcher of the XENON collaboration (Ted Berger). It selects events with at least two interactions (two S1 and S2 signals). Afterwards, the most intense S1 and S2 signals are ordered in times and the interaction information (e.g. the position of the interaction, the intensity of the peak...) are determined.

The different variables that will be used in the rest of this report are :

- **S1_a** as the first (in time) main S1 signals, which should correspond to the 32.2 keV-level decay according to the decay scheme 3.1. **S2_a (PE)** as the first (in time) main S2 signal, which should correspond to the sum of the two ^{83m}Kr radiations (= 41.6 keV), since S2 signals are not separated.

²Study performed on March, 2017

³Even if it would have been very interesting to study (for determine the Charge Yield at 9.4 keV and 32.2 keV for exemple).

- **S1_b** (PE) as the second (in time) main S1, which should correspond to the 9.4 keV-level decay.
- **S2_b** (PE) as the second (in time) main S2 signal, which should correspond to background events. Indeed, if S2_a is a pileup of a ^{83m}Kr decay, S2_b can only be background event or produced by the decay of an other atom of ^{83m}Kr .
- **Dt** (ns) as the delay time between the two radiations (S1_b and S1_a).
- **Δt** as the drift time, i.e. the time between S2_a and S1_a
- **s1_distinct_channels** as the number of PMTs contributing to S1_b distinct from the PMTs that contributed to S1_a

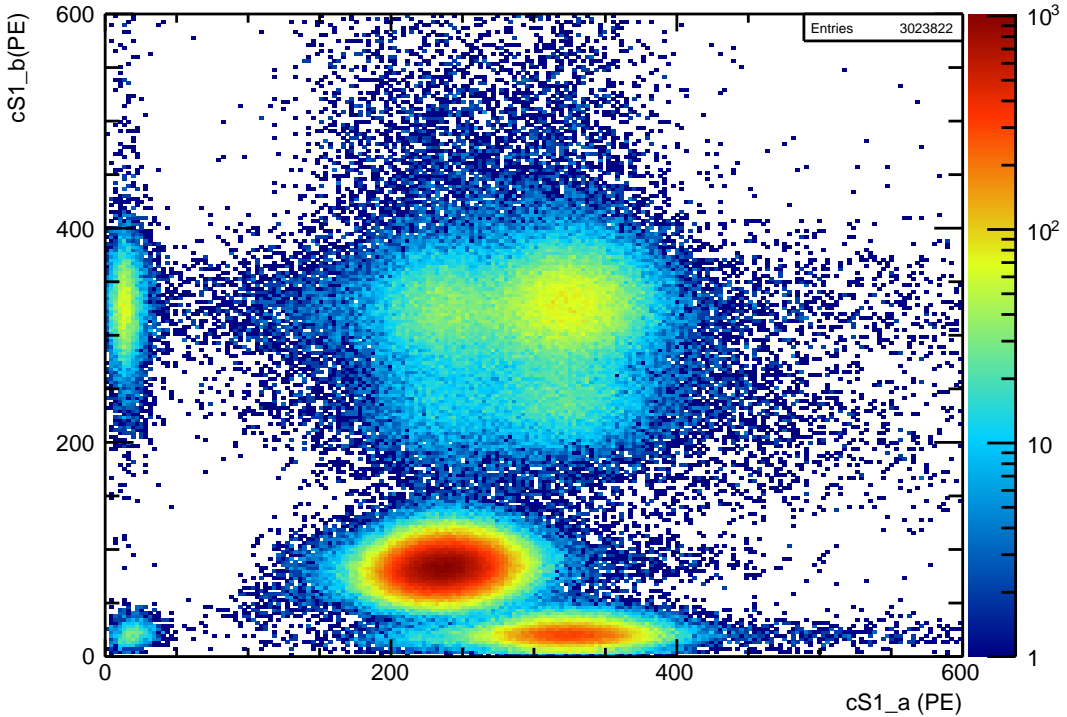


Figure 3.3 – S1_b as a function of S1_a without any selection cut.

In Figure 3.3, where the S1_a as a function of S1_b is shown, different populations of events appear. Based on the ^{83m}Kr decay characteristics and making the **first approximation of a linear response of the detector with the energy**: we should have $S1_a \approx 3 * S1_b$ for a ^{83m}Kr decay since $32.2 \text{ keV} \approx 3 * 9.4 \text{ keV}$.

Therefore, the population of events in the region ($S1_a = 250 \text{ PE}$, $S1_b = 90 \text{ PE}$) corresponds to ^{83m}Kr decay with S1_a as the S1 signal produced by the 32.2 keV-level decay and S1_b as the S1 signal produced by the 9.4 keV-level decay. In the rest of this report, this population will be called: **^{83m}Kr population**.

The aim of the next sections is to isolate this population from the "background populations" (that are presented below) in order to study the detector response at 32.2 keV and 9.4 keV, region of interest for DM search.

Single electrons charge signals are mainly induced by photoelectric effect of ultraviolet photons from a previous S2 signal over impurities in LXe or over metallic components of the TPC. Single electrons have a low energy and are visible in the region ($S1_a = 20 \text{ PE}$, $S1_b = 20 \text{ PE}$) [3].

To categorize the other populations, we can notice that the higher S1 signals should be produced during pileup and should correspond the sum of the two radiations (i.e. 41.6 keV). In Figure 3.3, the higher S1 is equal to 340 PE (i.e. $250 + 90 \text{ PE}$).

Therefore, the population with $S1_a = 340$ PE and $S1_b = 20$ PE corresponds to an event with the first S1 signals as a pileup event, and with the second S1 as electronic noise. The exact inverse population can be seen with $S1_b = 340$ PE and $S1_a = 20$ PE.

In Figure 3.3, in the region ($S1_a \approx 300$ PE, $S1_b \approx 300$ PE), we have a population where two ^{83m}Kr atoms decays at the same time, giving the 4 possibilities where the signal is either a pileup event or a 32.2 keV signal.

3.1.3. Events selection

To select the ^{83m}Kr population, we will perform different cuts. The first one is the selection of a fiducial volume, used to reduce the ambient radioactivity contamination. The second one is the cut on the number of distinct PMTs between $S1_b$ and $S1_a$ signals, used to cut the afterpulse and the electronic background. Finally, the cut on the delay time is used to reduce the electronic noise and the pileup of the S1 signals.

3.1.3.1. Fiducial Volume Cut

For DM search, the selection of a fiducial volume, spaced from edge of the detector⁴ by approximately 20 cm, is used to reduce the ambient radioactivity, mostly present at the edge of the detector.

During an internal calibration, the ^{83m}Kr is uniformly distributed inside the TPC, thus, the fiducial volume chosen will **not be contaminated by ambient radioactivity** and will only contain events coming from the ^{83m}Kr decay.

3.1.3.2. Cut on the Number of PMTs

The cut on the Number of PMTs contributing to the second S1 distinct from the PMTs that contributed to the first S1 allows the cut of afterpulses.

Afterpulse are generate **inside PMTs**, and only if an initial signal hits the PMTs. Afterpulses of short delay (tens of ns) are caused by elastic scattering electrons on the first dynode of the PMT. Afterpulses with longer delay are caused by positive ions which are generated by the ionization of residual gases in the PMT. These positive ions return to the photocathode and produce many photoelectrons the PMT [23].

Therefore, afterpulses are mostly reconstructed as **second signal** and will be seen in **only one PMT**, while real signal are seen on different channels: we ask an minimum of **3 distinct channels** between $S1_b$ and $S1_a$ signal.

3.1.3.3. Delay Time cut

In order to study the detector response at low energy, we want to **precisely measure** the 32.2 keV and 9.4 keV S1 signals. However, if the time between the two radiations of the ^{83m}Kr decay is two small, PMTs can be still "occupied" measuring the first signals when the second is emitted. $S1_a$ and $S1_b$ signals will not be correctly evaluated, and their reconstructed energies will not be exactly equal to 32.2 keV and 9.4 keV. The 9.4 keV S1 signal is emitted after the 32.2 keV decay, therefore, it is the one that suffers the most of the proximity issue.

We can notice that both of the S1 signals are expected to be constant over time (since it depends only of the energy deposit and thus the radioactive decay). Since it is more likely at small delay time than at large one, S1 signals (in particular $S1_b$) will not be constant over time when this phenomenon of signal proximity occurs.

A study of the 9.4 keV S1 signal as a function of the delay time will permit us to determine the time range where this contamination do not impact it (i.e. where the $S1_b$ is constant over time).

Figure 3.4 shows the $S1_b$ signal as a function of the delay time. The blue dots correspond to the mean values of the considered signal for each slice in delay time. The procedure is presented in

⁴The TPC is a ≈ 100 cm long by ≈ 100 cm wide cylinder

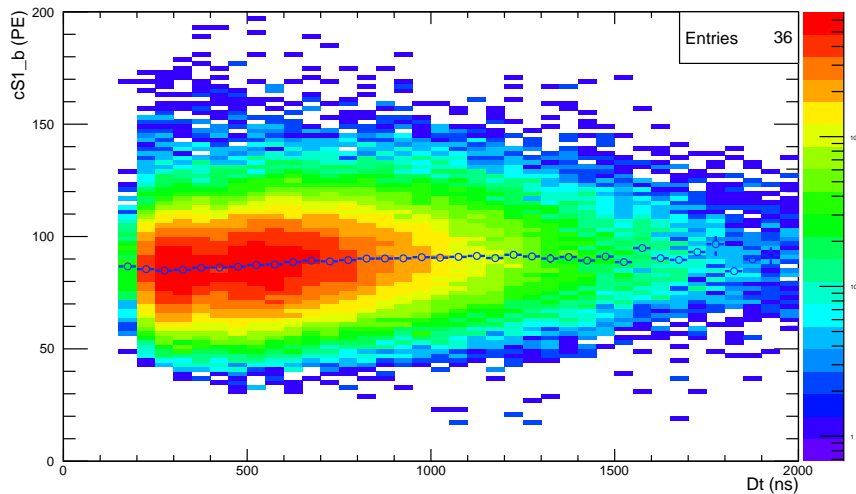


Figure 3.4 – S1 signals at 9.4 keV as a function of the delay time. The blue dots are the mean values of the Light Yield in each delay time slice.

detail in Appendix A and consists of taking the mean value of a Gaussian fit applied in each delay time slice. The delay time range where the S1_b signal is constant over time is between **1 000 and 1 500 ns**. The reduced $\tilde{\chi}^2$ of a linear fit applied on this range is $\tilde{\chi}^2 \approx 4.3$.

The reduced $\tilde{\chi}^2$ is the χ^2 divide by the number of degrees of freedom (NDF).

$$\tilde{\chi}^2 = \frac{\chi^2}{NDF} \quad (3.1)$$

When a distribution is fitted, if $\tilde{\chi}^2$ is smaller or in the order of the unity, it gives a good indication of the consistency between the fit and the distribution.

The S1_a signal is not as much constrained in time as the S1_b, therefore, we chose to study it for a delay time between **600 and 1 500 ns**⁵, which is the usual cut for ^{83m}Kr calibration.

Finally, Figure 3.5 shows S1_b as a function of S1_a for events with a delay time bigger than 1 500 ns. It allows to verify that pileup populations are mostly present for large delay times, while the ^{83m}Kr population is spared by this cut. Indeed, since a delay time of 1 500 ns correspond to approximately 10 times the average time between the two radiations, if the first S1 signal corresponds to a ^{83m}Kr decay (i.e. S1_a = 32.2 keV), it is highly unlikely that the second S1 signal is the 9.4 keV signal⁶.

3.1.3.4. Conclusion

In Figure 3.6, S1_b as a function of S1_a is shown after applying all cuts listed in Table 3.2, showing the selected ^{83m}Kr population where S1_a is the signal produced by the 32.2 keV-level decay and S1_b is the signal produced by the 9.4 keV-level decay.

Fiducial Volume	$0 < R^2 < 1\,000 \text{ cm}^2$ and $-80 < Z < -20 \text{ cm}$
Number of Distinct PMT	s1_distinct_channels > 3
Delay Time	$600/1\,000 < Dt < 1\,500 \text{ ns}$

Table 3.2 – Lists of the Cuts used to select the ^{83m}Kr population

⁵The $\tilde{\chi}^2$ of a linear fit applied on this range is ≈ 3 .

⁶S1_b corresponds to an electronic background noise or to the decay of an other ^{83m}Kr atoms.

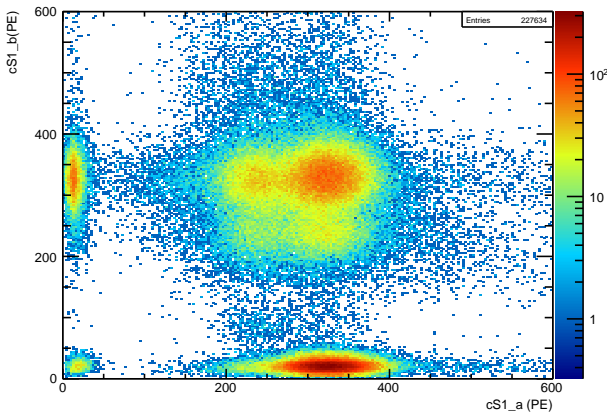


Figure 3.5 – S1_a vs S1_b for events with $Dt > 1\ 500$ ns, showing that pileup populations are mostly present for large delay times.

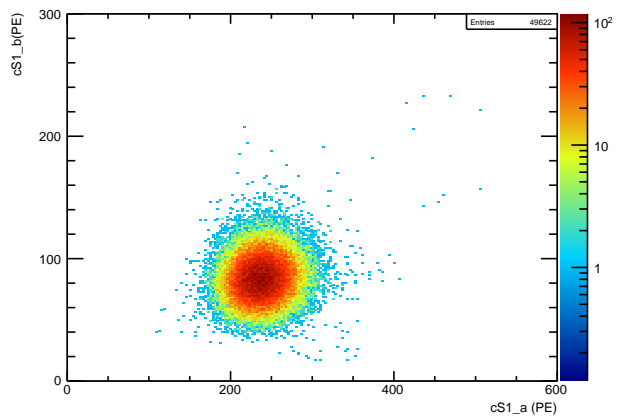


Figure 3.6 – S1_a vs S1_b after cuts listed in Table 3.2

3.2. Determination of Calibration Quantities

Once the selection cuts are applied, we have a clean ^{83m}Kr population with :

- S1_a corresponding to an energy of 32.2 keV
- S1_b corresponding to an energy of 9.4 keV
- S2_a corresponding to an energy of 41.6 keV

In the rest of this Chapter, we will determine the **Ligh Yield at 32.2 keV and 9.4 keV**, the **Charge Yield at 41.6 keV**, the **Electron Lifetime and the Energy Resolution**.

3.2.1. Light Yield

The Light Yields are equal to the S1 signals dividing by the corresponding energy, as indicated in equation 3.2.

$$Ly_{32.2} = \frac{S1_a}{32.2 \text{ keV}} \quad \text{and} \quad Ly_{9.4} = \frac{S1_b}{9.4 \text{ keV}} \quad (3.2)$$

The Light Yields are calculated using their evolutions with the delay time: the mean value of the Light Yields in each delay time slice is provided by a Gaussian function fit, as shown in Appendix A. Then, a linear fit is applied on the mean data points, giving the final Light Yield values⁷. For S1_a signal, the linear fit is provided between 600 and 1 500 ns, while it is provided between 1 000 and 1 500 ns for S1_b signals, as shown in section 3.1.3.3 (see Appendix B).

We applied the same method on several calibration campaigns (from the February 13th, 2017 to the May 16th, 2017), in order to provide an off-line monitoring of the XENON1T detector. Each campaign correspond to ≈ 24 hours of data taking. The evolutions of the Light Yield (at 32.2 keV and 9.4 keV) over time are shown and commented in Appendix C (Figures C.1, C.2).

The Light Yields at 32.2 keV and 9.4 keV are **stable during the few months studied**, shown by the χ^2 of the linear fit, equals to ≈ 6 at 32.2 keV and ≈ 0.4 at 9.4 keV, smaller or of the order of the unity. Since it has bigger error bars⁸, the Light Yield at 9.4 keV has a smaller χ^2 than the Light Yield at 32.2 keV.

⁷The results obtained with this method was cross-check with the results obtained by only fitting the Light Yield distributions with a single Gaussian.

⁸The Light Yield at 9.4 keV was calculated using a linear fit on delay time slices (i.e. $Dt > 1\ 000$ ns) where the statistic was low. The systematic errors, that come from the slice per slice Gaussian fits, are bigger than on more populated slices.

The stability of the S1 signals is one of the purpose for DM search. The average values of the Light Yields over the three month studied are given in Table 3.3.

Energy (keV)	Light Yield (PE/keV)	χ^2/NDF
32.2	7.849 ± 0.002	43.6 / 7
9.4	9.700 ± 0.039	2.7 / 7

Table 3.3 – Light Yield results for the calibration campaigns between the February, 13th and the May, 16th. Both statistic and systematic errors are indicated. The systematic errors come from the slice per slice Gaussian Fit (see Appendix A).

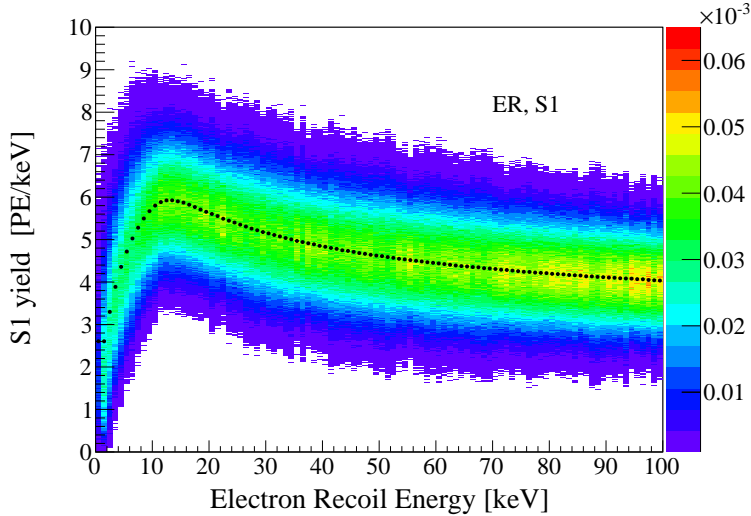


Figure 3.7 – Monte-Carlo simulation of the distribution of the S1 (Light) yield as a function of the deposited energy. The z-axis is expressed by the colors in terms of normalized units, the same number of events has been generated in each 1 keV slice of the x-axis. The black dots represent the mean value of the signal yield in each energy slice [24]

We can notice that the Light Yield at 9.4 keV is bigger than the one at 32.2 keV, which is consistent with the trend of the monte-carlo simulation of XENON1T for ER, shown in Figure 3.7. Besides, we can compared our result with other experiments ([25], [26], [27] and [28]) thanks to the Light Yield ratio when no electric field is applied in the TPC: $R_{Ly}(\vec{0} \text{ (V/cm)})$.

$$R_{Ly}(\vec{0} \text{ (V/cm)}) = \frac{Ly_{9.4 \text{ keV}}(\vec{0} \text{ (V/cm)})}{Ly_{32.2 \text{ keV}}(\vec{0} \text{ (V/cm)})} \quad (3.3)$$

To determine the Light Yield with no electric field, we use the Thomas-Imel box model. It allows determination of the quenching factor $q(E, \vec{E}_f)$, that takes account of the electric field in the TPC [26]. The Thomas-Imel bow model relies on the assumption that each electron-ion pair produced by an interaction in LXe is isolated from all other, uniformly distributed in a box, and only subjected to the drift field [29].

Based on this model [26], the Light Yield when no electric field is applied is:

$$Ly(E(\text{keV}), \vec{0} \text{ (V/cm)}) = \frac{Ly(E(\text{keV}), \vec{E}_f(\text{V/cm}))}{q(E(\text{keV}), \vec{E}_f(\text{V/cm}))} \quad (3.4)$$

Where \vec{E}_f is the field strength and E is the radiation's energy.

The **quenching factors** are:

$$q(32.2 \text{ keV}, \vec{0} \text{ V/cm}) = 0.89 \pm 0.04 \text{ and } q(9.4 \text{ keV}, \vec{0} \text{ V/cm}) = 0.95 \pm 0.06.$$

$$\text{We obtain: } R_{Ly}(\vec{0} \text{ V/cm}) = (1.16 \pm 0.11) \text{ PE/keV.}$$

For comparison, measurements of this ratio for different studies are given in Table 3.4. We note that our measurement is a higher then the others, but consistent in the error bars.

Authors (Year)	$\mathcal{R}_{L_y}(\vec{0} \text{ (V/cm)})$	Ref.
Kastens et al. (2009)	0.976 ± 0.001	[25]
Manalaysay et al. (2010)	1.056 ± 0.011	[26]
Aprile et al. (2012)	1.052 ± 0.005	[27]
Baudis et al. (2013)	1.100 ± 0.004	[28]
THIS WORK (2017)	1.159 ± 0.112	—

Table 3.4 – Ratio of light yields at 9.4 keV and 32.2 keV at zero field measured in several studies

3.2.2. Charge Yield

The Charge Yield is equal to the S2 signals dividing by the corresponding energy as shown in equation 3.5.

$$Cy_{41.6} = \frac{S2_a}{41.6 \text{ keV}} \quad (3.5)$$

As a reminder, the S2_a signal corresponds to the sum of ^{83m}Kr radiations ($= 41.6$ keV), since the time width of S2 signals is too large to separate the two radiations from each other.

Note that, since the S2 signal is produced close to the top array of PMTs, some of them can saturate [19]. To avoid a loss of information, it is common in the XENON collaboration to use the S2 bottom signal, which is the corrected area of the S2 signal measured by the bottom array of PMTs.

The Charge Yield is calculated using its evolution with the delay time as shown in Appendix B (Figure B.3), in the same way as for the Light Yields.

We applied the same procedure on several calibration campaigns (from the February 13th, 2017 to the May 16th, 2017). The evolution of the Charge Yield over time is shown in Figure 3.8. Figure 3.8 shows that the Charge Yield **increases** by $\approx 2.5\%$ between February and April, 2017. The behaviour can be induced by an incorrect Electron Lifetime correction of the S2 signal (see section 2.3). Therefore, in the next section, we will compute and monitor the Electron Lifetime.

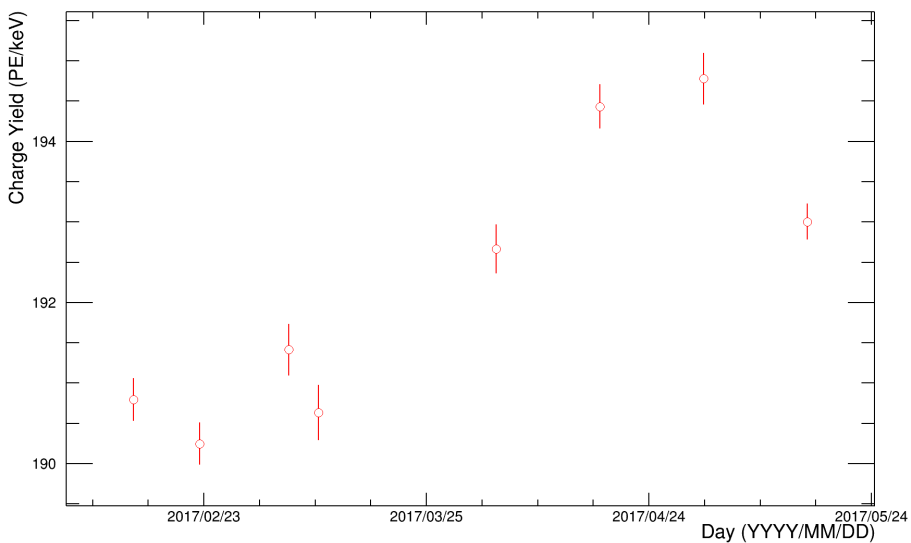


Figure 3.8 – Charge Yield at 41.6 keV as a function of the time. Each point corresponds to ≈ 24 hours of calibration data taking. For each calibration campaign, the Charge Yield was determined with the method presented in this section. The errors bars include the statistic and the systematic errors.

3.2.3. Electron Lifetime

The Electron Lifetime is one of the **correction applied on S2 signals**. The Electron Lifetime also allows a measurement of the **impurity concentration** (see section 2.3). Therefore, it is extremely important to know its value during all the operation of XENON1T.

To calculate the Electron Lifetime, we study the main uncorrected⁹ S2 signal as a function of the electrons Drift Time (Δt). As for the Charge Yield, we use the S2 signal measured by the bottom array of PMTs (S2_a_bottom). Figure 3.9 shows an example of the Electron Lifetime determination for the calibration campaign of the February, 22th and 23th, 2017. The mean values of S2_a_bottom in each slices in Drift Time¹⁰ are calculated and a exponential fit (see equation 2.5) is applied on these mean values. With this method, we obtain an Electron Lifetime equals to $(581.73 \pm 4.84) \mu\text{s}$, which is consistent with values obtained by the XENON collaboration.

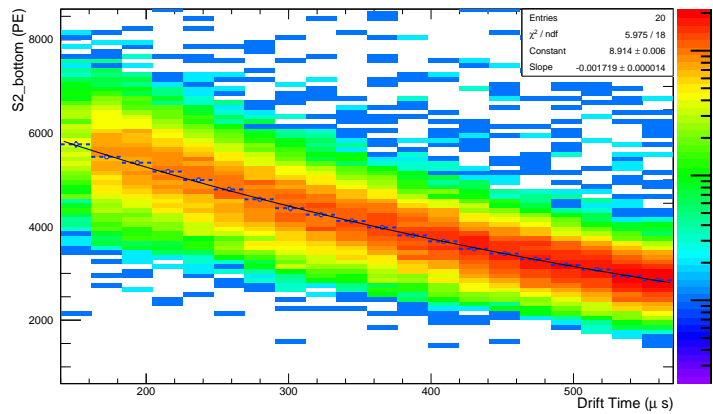


Figure 3.9 – S2_a_bottom as a function of the Drift Time, the cuts used are listed in Table 3.2. The dataset was taken the February, 22th and 23th, 2017. The blue dots are the mean values of S2_a_bottom in each Drift Time slice. We can find this figure in a larger size in Appendix B. The exponential fit, shown by the black line, allows the determination of the Electron Lifetime.

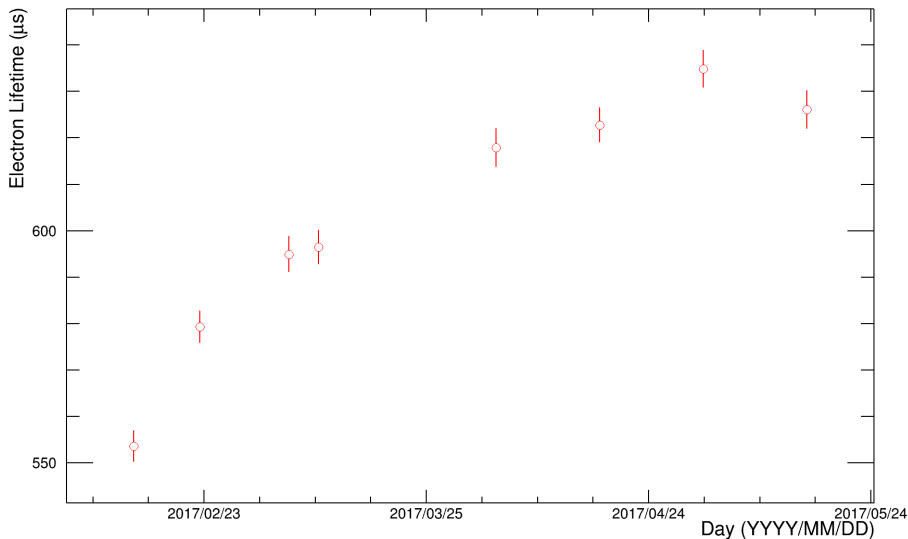


Figure 3.10 – Electron Lifetime as a function of the time. Each point corresponds to ≈ 24 hours of calibration data taking. For each calibration campaign, the Electron Lifetime was determined with the method presented in this section. The errors bars include the statistic and the systematic errors.

We applied the same procedure on several calibration campaigns (from the February 13th, 2017

⁹We use the uncorrected S2 signal because the Electron Lifetime is one of the correction applied of S2 signals.

¹⁰The mean values of S2_a_bottom in each drift time slice were calculated using a Gaussian fit.

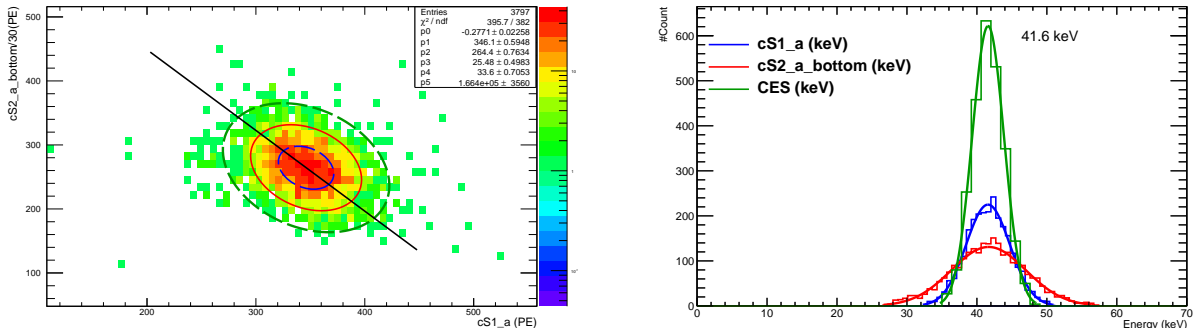
to the June 7th, 2017). The evolutions of the Electron Lifetime over time is shown in Figure 3.10. The Electron Lifetime **increased** by $\approx 9\%$ from February to May. This behaviour is induced by **improvement on the purification system**. Indeed, as saw in section 2.3, the Electron Lifetime depends on the number of impurities in the LXe, the less impurities are in the LXe, the higher the Electron Lifetime is.

The augmentation of the Electron Lifetime explain why the Charge Yield increase on the same period, as seen in Figure 3.8 and based on equation 2.5.

3.2.4. Energy Resolution

An other essential quantity used to characterize the detector response to an energy deposit is the Energy Resolution of the measurement. As we saw in section 2.2, the production of the S1 and S2 signals are anti-correlated: a large S2 means a small S1. Using a combination of these two signals (i.e. the combined energy scale (CES)) reduces the fluctuation of the individual signal and gives a better resolution of the measured energy than individual S1 or S2 signal [19].

$$CES = aS1 + bS2 \quad (3.6)$$



(a) S2_a_bottom as a function of S1_a, at 41.6 keV. The ellipse is fit by a two dimensional gaussian function, allowing the determination of the anti-correlation angle between S1_a and S2_a_bottom. The projection of the energies along the large axis of the ellipse is indicated by the blue line. The ellipses in blue, red and green, indicate respectively the 2D-Gaussian fit at 1,2 and 3 σ . The events present "outside" the 3 σ ellipse are cut from the dataset. We can find this figure in a larger size in Appendix B

(b) Distribution of the CES, S1_a and S2_a_bottom energies at 41.6 keV. The Gaussian fit, applied on each distribution, allows the determination of the Energy Resolution.

Figure 3.11 – Determination of the Energy Resolution at 41.6 keV for the calibration campaign of the February, 22th and 23th, 2017.

In Figure 3.11a, the CES is the projection of the S1 and the S2 energies along the large axis of the ellipse formed in the S1 against S2 plan. To do this projection, we need to determined the anti-correlation angle between S1 and S2, gave by the two dimensional Gaussian function fit.

In our case, since the two S2 signals of the ^{83m}Kr decay are not separated, **the CES can only be determined at 41.6 keV**: we select from our dataset the population with one S1 signal (one S1 and one S2 population in Table 3.1).

To select this population, we inverse the selection cut on the Number of PMTs (see section 3.1.3.2): $s1_distinct_channels \leq 3$. This new cut allows the selection of the population where S1_b is an afterpulse, and thus, where S1_a is an pileup event, with the desired energy of 41.6 keV.

One the CES is computed at 41.6 keV, we apply an 1D-Gaussian fit on its distribution in order to determine its **Energy Resolution**, as show in Figure 3.11b. Indeed, the Energy Resolution (R) is define as :

$$R = \frac{\sigma}{\mu} \quad (3.7)$$

Where σ is the standard deviation and μ the mean value of the distributions, determined by the 1D-Gaussian fit.

We applied the same procedure on several calibration campaigns (from the February 13th, 2017 to the May 16th, 2017). The evolutions of the Energy Resolution over time are shown in Appendix C (Figure C.5). The Energy Resolutions of S1_a, S2_a and of the CES are given in Table 3.5: they are stable during the three months studied (as indicated by the $\tilde{\chi}^2$ of the linear fit, respectively equal to 0.3, 0.09 and 1.1: smaller or consistent with the unity).

As intended, **the CES improve the energy resolution of XENON1T.**

	Resolution at 41.6 keV (%)	χ^2/NDF
CES	5.46 ± 0.03	7.51/7
S1_a	7.67 ± 0.08	2.3/7
S2_a_bottom	13.41 ± 0.11	0.65/7

Table 3.5 – Energy Resolution for the calibration campaign from the February 13th, 2017 to the May 16th, 2017. The errors contains systematic and statistic ones.

The **CES Energy Resolution is stable** on the three month studied, with an average values of $5.46 \pm 0.03\%$. The stability of the Energy Resolution of the detector is important and is one of the objective for DM search.

3.2.5. Conclusion

In this Chapter, we studied the stability of the XENON1T detector through the calibration at low-energy using a ^{83m}Kr source.

We provided the monitoring of the Light Yield at 32.2 keV and 9.4 keV, the Charge Yield at 41.6 keV, the Electron lifetime and the Energy Resolution.

The increase of the Electron Lifetime is consistent with the XENON collaboration, and explain why the Charge Yield increase on the same period.

The stability of the Light Yield and of the Energy Resolution of the XENON1T is an important and necessary objective for DM search.

The methods presented in this chapter can be used on other studies. One of them is the study of the detector response when different drift fields are applied in the TPC and will be started in the next Chapter.

Study at different electric fields

In the previous Chapter, we provide valubles methods to determine the Light Yield, the Charge Yield, the Electron Lifetime and the Energy Resolution of XENON1T. In this Chapter, we will apply these methods for different drift fields, allowing the study of the detector response under different field configurations, especially at low one.

One advantage of decreasing the drift field is to increase the detection efficiency of low-mass WIMP. Indeed, if the drift field decreases, the S1 signal will be more intense (see section 2.2¹). The S1 signals have a lower intensity than S2 signals. Therefore, if we increase the S1 signal, the detection efficiency of lower-energy WIMP-nucleus interaction (and thus the detection of low-mass WIMP) will be increased.

On February, 2017, the XENON collaboration took ^{83m}Kr data with lower drift fields: **40 V/cm**, **50 V/cm**, **60 V/cm**, **70 V/cm**, **80 V/cm**. An additional dataset with a drift field of 120 V/cm (recorded the November, 14th 2016) is used.

4.1. Uncorrected Signals

We have to notice that we can not use corrected signals in this Chapter. Indeed, as we saw in section 2.3, corrections depend on the position of the interactions, but the position reconstruction itself depends on the drift field applied in the TPC, in particular for the Z coordinate, as shown in equation 4.1. The XENON collaboration produces correction for standard drift field. Therefore, the S1 signals used in the rest of this Chapter will not be corrected². The S2 signals will only be corrected with the electron lifetime (that we will determine ourself in section 4.3).

In the same way, to provide the Fiducial Volume cut, we need to calculated the Z coordinate.

$$Z = v_d \cdot \Delta t \quad (4.1)$$

$$v_d = \frac{Z_{max}}{\Delta t_{max}} \quad (4.2)$$

Where v_d is the **drift velocity** of the electrons.

For each drift field applied in the TPC, we computed v_d using equation 4.2, where Z_{max} is the maximal Z position, and thus equals the height of the TPC ($Z_{max} = 96.9\text{ cm}$), and where Δt_{max} is the maximal Drift Time that is determined for each drift field (see Annexe D).

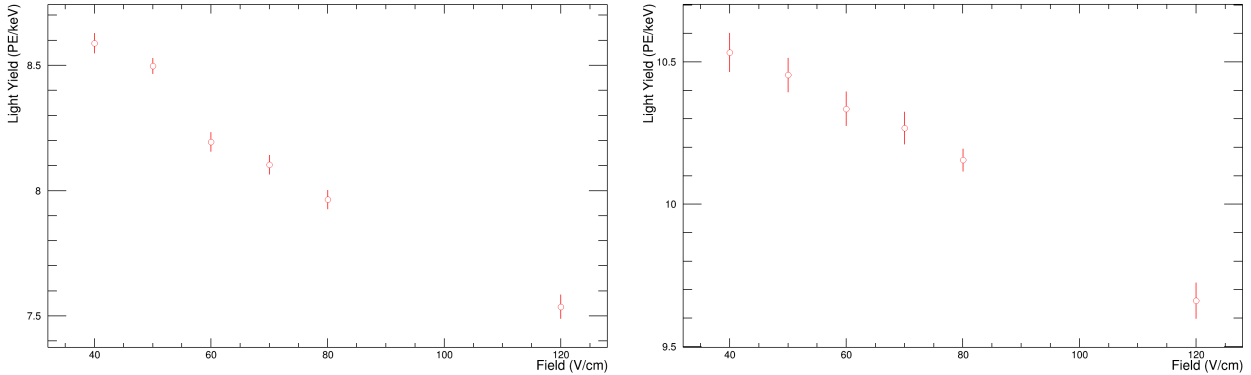
4.2. Light Yields dependence with the electric field

The evolution of the Light Yields at 32.2 keV and 9.4 keV are given in Figures 4.1a and 4.1b. You can find these Figures in a larger size in Appendix E.

The Light Yield decrease when the electric field increase, as expected. Indeed, the S1 and S2 signals depend on the number of electrons that escape the recombination with xenon atoms. The stronger

¹As a reminder, the S1 signal depends on the number of electrons that do not escape the recombination. The smaller the drift field, the less electrons can escape it, giving a bigger S1.

²The dependence of S1 signal with the Z position is neglected



(a) Light Yield at 32.2 keV as a function of the drift field applied in the TPC (b) Light Yield at 9.4 keV as a function of the drift field applied in the TPC

Figure 4.1 – Each point corresponds at ≈ 2 hours of calibration data taking. For each point, the Light Yields is determined with the method presented in section 3.2.1. The errors bars include the statistic and the systematic errors.

the electric field is, the more electrons can escape the recombination, giving a more intense S2 signal, but a less intense S1 signal, and thus a smaller Light Yield (see section 2.2). The Light Yield at 32.2 keV decrease by $\approx 12\%$, and the Light Yield at 9.4 keV decrease by $\approx 9\%$.

4.3. Charge Yield and Electron Lifetime dependence with the electric field

To determine the Charge Yield, we will apply the same method as in section 3.2.2. However, we will first correct the S2 signals using the Electron Lifetime (see equation 2.5). The Electron Lifetime for each field is determined using the same methods as in section 3.2.3. Its evolution with the drift field is shown in Figure 4.2a. You can find this Figure in large size in Appendix E.

We can see that between 40 and 80 V/cm, the Electron Lifetime is **stable**, with an average value of (531.72 ± 2.13) μ s (and with a χ^2 of 0.86, smaller than the unity), which was expected since the Electron Lifetime do not depend on the drift field, but only on the number of impurities. The Electron Lifetime decrease³ at 120 V/cm because the number of impurities decrease from November 2016 to February 2017. In all case, our Electron Lifetime is consistent with one provided by the XENON collaboration.

After applying the Electron Lifetime correction to S2 signals, we calculated the Charge Yield. The evolution of the Charge Yield with the drift field is shown in Figure 4.2b. You can find this Figure in large size in Appendix E.

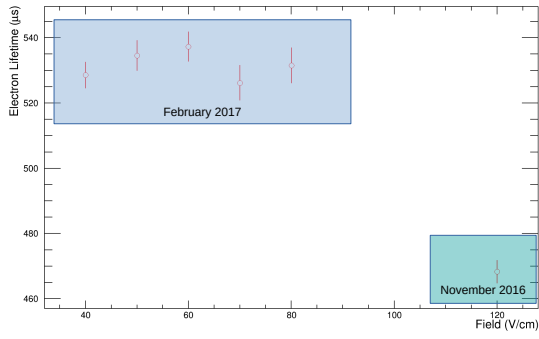
The Charge Yield **increase** (by $\approx 23\%$) with the drift field, as expected. Indeed, the Charge Yield depends on the number of electrons that escape the recombination with xenon atoms. The stronger the electric field is, the more electrons can escape the recombination, giving a more intense S2 signal, and thus a bigger Charge Yield. Besides, we verified that the Charge Yield increase when the Light Yield decrease (see section 2.2).

4.4. Energy Resolution dependence with the electric field

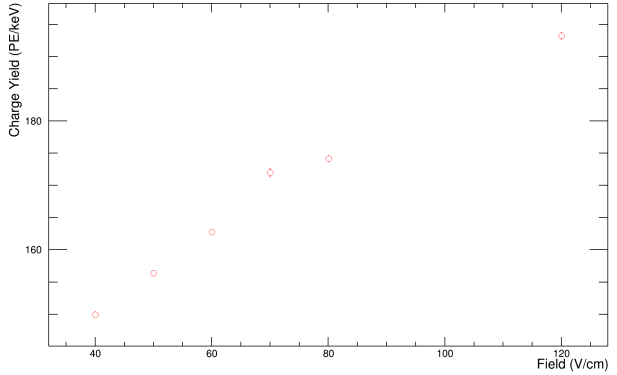
The evolution of Energy Resolution (of the S1, S2 signals and of the CES at 41.6 keV) as a function of the drift field is shown in Appendix E (Figure E.5). We calculate the CES with the same method as in section 3.2.4, with the S2 signals corrected using the Electron Lifetime⁴, based on equation 2.5.

³The dataset at 120 V/cm was recorded in November 2016.

⁴The Electron Lifetime was calculated in the previous section



(a) Electron Lifetime as a function of the drift field applied in the TPC. Boxes indicate the date and the expected value from the Electron Lifetime corresponding to the purity at the time of the data-taking.



(b) Charge Yield at 41.6 keV as a function of the drift field applied in the TPC

Figure 4.2 – Each point corresponds at ≈ 2 hours of calibration data taking. For each point, the Charge Yield and the Electron Lifetime is determined with the method presented in sections 3.2.2 and 3.2.3. The errors bars include the statistic and the systematic errors.

The Energy Resolutions of S1, S2 signals and CES at 41.6 keV are **stable** with the drift field applied in the TPC (χ^2 smaller or in the order of the unity). The average values obtained by the linear fits are given in Table 4.1. The evolution of the Energy Resolution is under investigation and will be compared with Monte Carlo simulation data.

	Resolution at 41.6 keV (%)	χ^2/NDF
CES	8.2 ± 0.12	7.3/5
S1_a	13.02 ± 0.23	3.8/5
S2_a_bottom	13.44 ± 0.27	2.19/5

Table 4.1 – Average value of the Energy Resolutions, for different drift field. The errors contains systematic and statistic ones.

4.5. Conclusion

In this Chapter, we started an analysis of the XENON1T detector response at different drift field. **We verify that the Light Yield decrease, while the Charge Yield increase with the drift field.**

We also study the Energy Resolutions at 41.6 keV. In the rest of my internship, I will start a **Monte Carlo simulation** production to study the detector response at different electric field. Afterwards, I will compare the simulation with the real data studied in this Chapter.

The first step of the Monte Carlo production will be to calculate the diffusion coefficient of the S2 signals. Indeed, when the drift field increase, the electrons cloud that reached the gas phase, is less widespread. The diffusion of the electrons' cloud is needed in Monte Carlo production in order to provide the right S2 signal shape.

Conclusion and Outlook

XENON1T, the third detector of the XENON collaboration, aims to detect low-energy nuclear recoil inducing by elastic scattering of Dark Matter particles with xenon nuclei. It is nowadays the most sensitive direct detection experiment to a spin-independent WIMP-nucleus interaction.

The **characterisation of the experiment** in the energy region of interest for Dark Matter search is possible with a ^{83m}Kr source, that emits two low-energy γ -rays (at 32.2 keV and 9.4 keV).

In this report, the calibration and the study of the stability of the XENON1T experiment using a ^{83m}Kr source is described. This work was performed in the XENON collaboration: all the results were cross-check with the one obtained by other researchers of the collaboration.

After the selection of the population corresponding to ^{83m}Kr decays, the **Light and Charge Yield** (conversion factors between the S1 (S2) signal and the deposit energy), the **Electron Lifetime** (allowing the measurement of the LXe purities) and the **Energy Resolution** of XENON1T were computed and used to study the stability of XENON1T. The Light Yield obtained in this work was successfully confronted with literature.

In order to maximize the probability of detecting a WIMP-nucleus interaction, XENON1T has to take data during several years. The stability of the detector is an important and necessary objective for DM search and was verified through the Light Yield and the Energy Resolution stabilities.

Afterwards, the detector response was studied under different electric field. The evolutions of the Light Yield, the Charge Yield and the Electron Lifetime as a function of the drift field was expected and verified that XENON1T can be used at lower drift field than the one used today. The evolution of the Energy Resolutions with the drift field has to be thoroughly investigated.

Therefore, in the rest of my internship, I will start a **Monte Carlo simulation** production to study the detector response at different electric fields. Afterwards, I will compare the simulation with real data provide by the XENON collaboration on February 2017.

Before the end of my internship, I will report my results from the analysis, and hopefully about the Monte Carlo study. We already started to exchange with the collaboration about my work. Besides, at the beginning of my internship, Julien Masbou presented to the collaboration my first analysis of the ^{83m}Kr decay in XENON1T⁵.

In the same time, I will continue to study the stability of XENON1T, by adding new ^{83m}Kr calibration campaign datasets to my off-line monitoring algorithm.

⁵Shown in Figure 3.2

Method used to compute the means values in slices

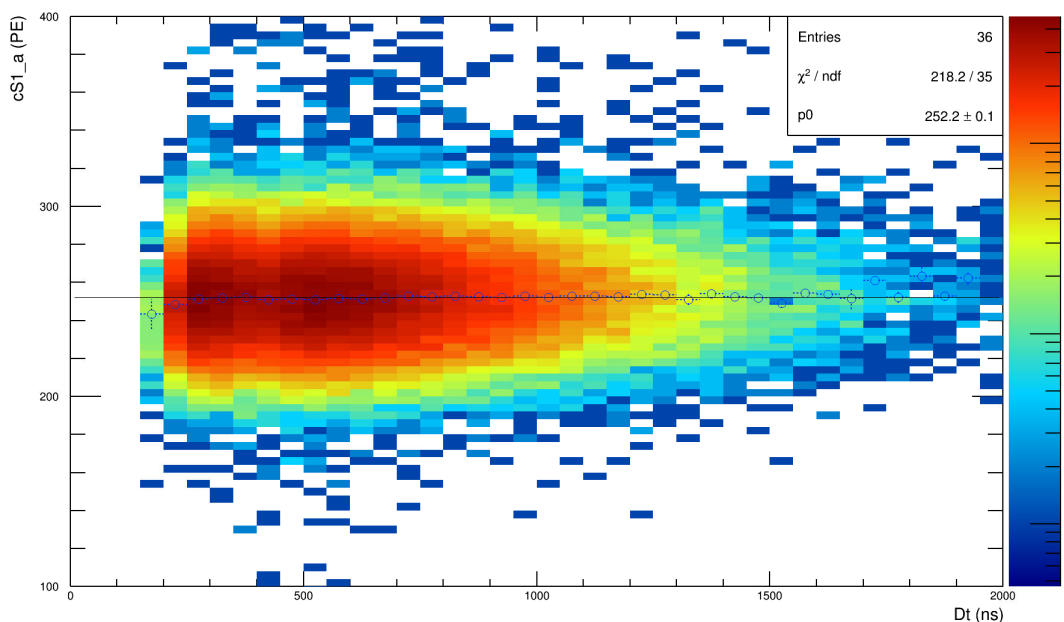


Figure A.1 – S1_a at 32.2 keV as a function of the delay time. Blue dots are the means values of the S1 signal for each delay time slice.

In this Appendix, the method used to study signal (S1 and S2) as a function of the delay time is presented. It allows to compute the Light and Charge Yield. This method is also applied to calculate the Electron Lifetime, but with S2 studied as a function of the Drift Time.

To present the procedure, we will take the example of the Light Yield at 32.2 keV (see Figure A.1):

- S1 signal as a function of the delay time (S1_a vs Dt) is drawn.
- In each slice of the x-axis (i.e. slice in delay time), S1_a distribution is fitted a first time with Gaussian function.
 - To avoid any error for the choice of the fitting ranges, an iterative procedure is used :
 - * We iteratively fit each distribution with a Gaussian function, which takes as parameters the values obtained with the previous fit, within the range :

$$[\mu_{n-1} - N_\sigma \sigma_{n-1}, \mu_{n-1} + N_\sigma \sigma_{n-1}] \quad (\text{A.1})$$

- * Where n is the current iteration, and N_σ is equal to 1,2 or 3 (i.e. the number of Gaussian σ). An example of Gaussian Fits are shown in Figure A.2.

- * The procedure is stopped when the converge condition is reached. This condition is

$$|\mu_n - \mu_{n-1}| < 2\Delta\mu_n \quad (\text{A.2})$$

- * Where $\Delta\mu_n$ is the statistical uncertainty associated to the mean μ_n

- The final mean value, for the considered slice, is μ_n . The associated statistical error is $\Delta\mu_n$ and the systematic one is defined as the maximal difference between the mean values resulting from the iterations.
- The Light Yield is obtained by fitting the S1 mean values (divide by the corresponding energy, see equation 3.2) as a constant with the delay time, as shown in Figure A.1

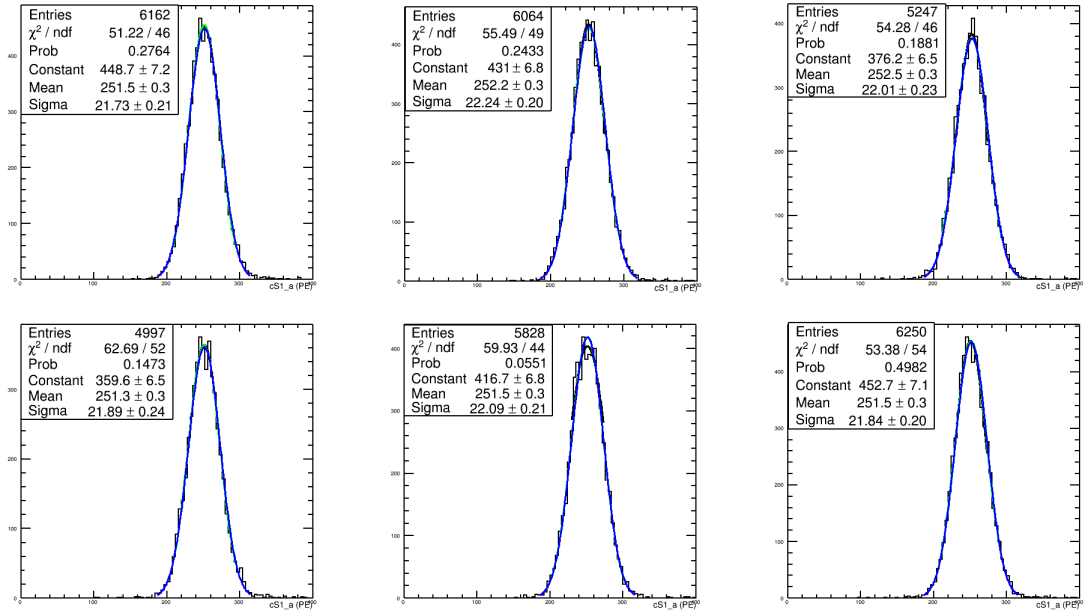


Figure A.2 – Gaussian Fit of the Light Yield distributions at 32.2 keV, for several delay time slices

Calibration Campaign of the February, 22th and 23th, 2017

In this appendix, an example of the calculation of the calibration quantities (i.e. Light Yield, Charge Yield, Electron Lifetime and Energy Resolutions) are calculated using the methods presented in Chapter 3. In all cases, the results of the fit used to determine these quantities are given in the Statistic Box, on each histogram. For each of them, the $\tilde{\chi}^2$ is smaller or in the order of the unity.

As a reminder, the reduced $\tilde{\chi}^2$ is the χ^2 divide by the number of degrees of freedom (NDF).

$$\tilde{\chi}^2 = \frac{\chi^2}{NDF} \quad (\text{B.1})$$

When a distribution is fitted, if $\tilde{\chi}^2$ is smaller or in the order of the unity, it gives a good indication of the consistence between the fit and the distribution.

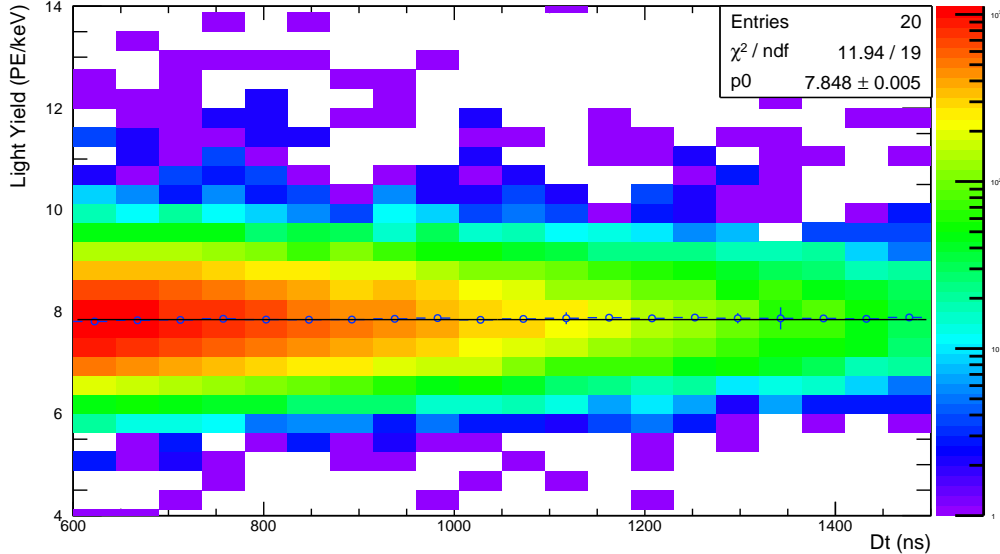


Figure B.1 – Light Yield at 32.2 keV as a function of the delay time, for the February, 22th and 23th, 2017. The blue dot are the mean values of the Light Yield in each delay time slice. The black line is the linear fit between 600 ns and 1 500 ns that allows the determination of the Light Yield.

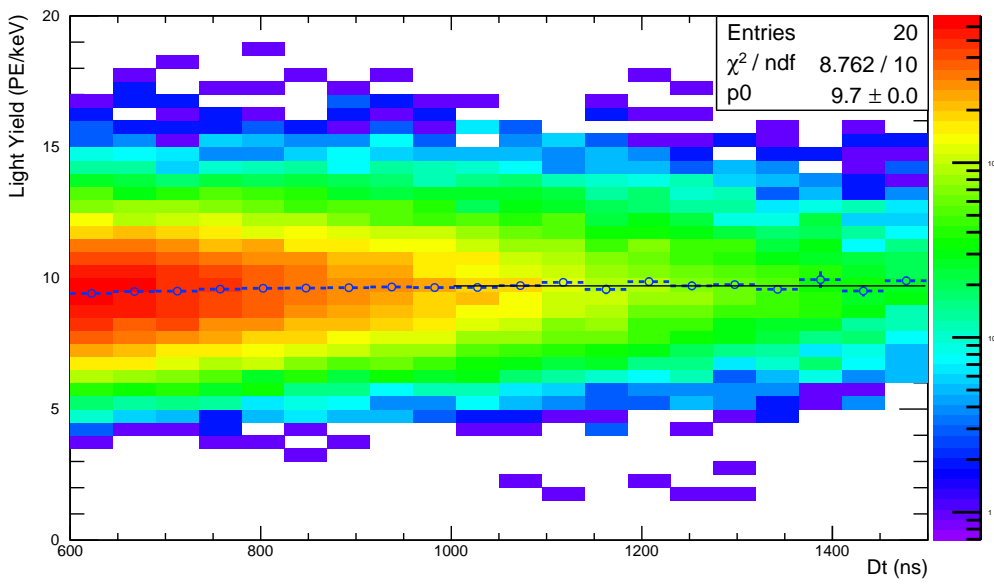


Figure B.2 – Light Yield at 9.4 keV as a function of the delay time, for the February, 22th and 23th, 2017. The blue dot are the mean values of the Light Yield in each delay time slice. The black line is the linear fit between 1 000 ns and 1 500 ns that allows the determination of the Light Yield.

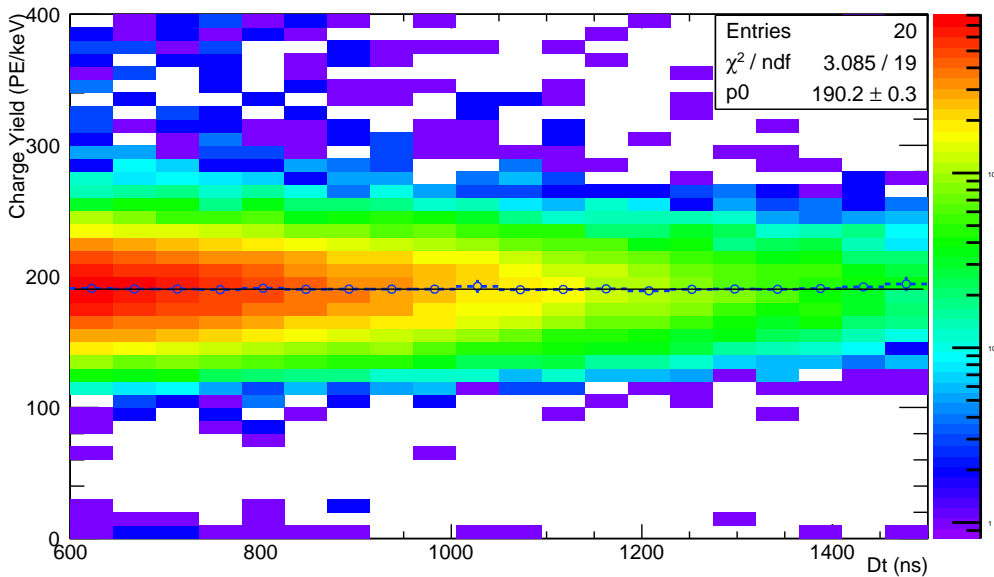


Figure B.3 – Charge Yield at 41.6 keV as a function of the delay time, for the February, 22th and 23th, 2017. The blue dot are the mean values of the Charge Yield in each delay time slice. The black line is the linear fit that allows the determination of the Charge Yield.

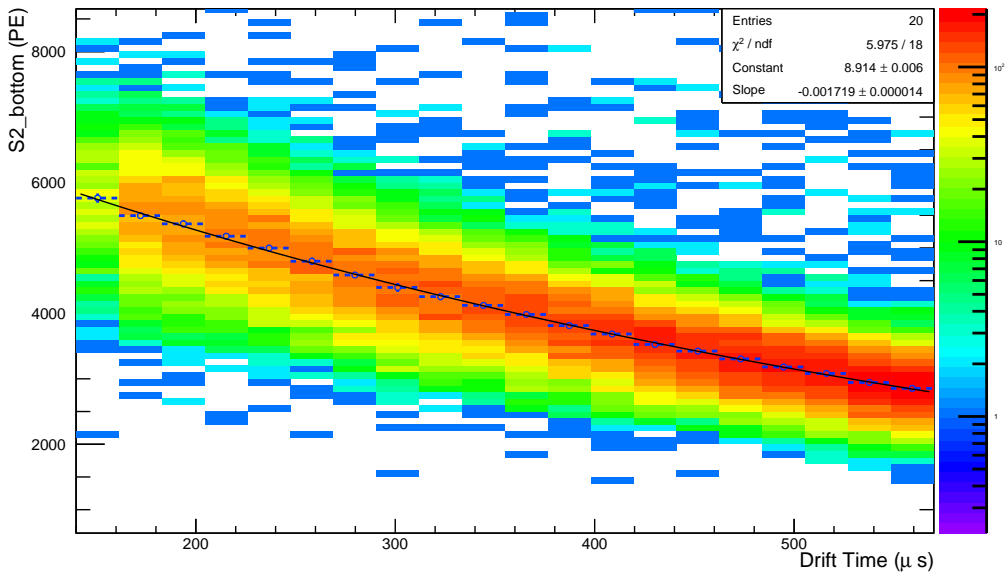


Figure B.4 – S2_a_bottom as a function of the Drift Time. The blue dot are the mean values of S2_a_bottom in each Drift Time slice. The black line is the exponential fit that allows the determination of the Electron Lifetime.

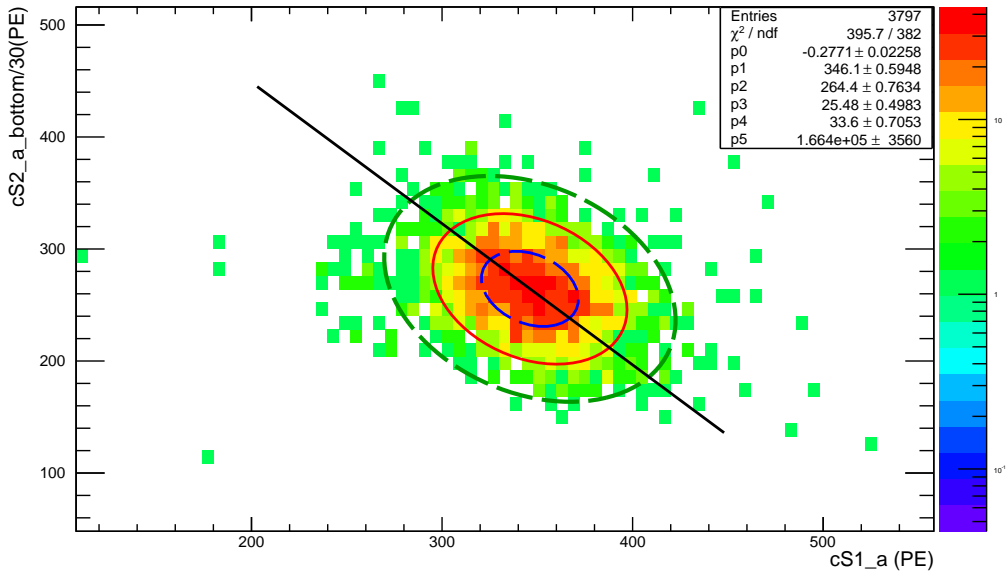


Figure B.5 – S2_a_bottom as a function of S1_a, at 41.6 keV. The ellipse is fit by a two dimensional Gaussian function, allowing the determination of the anti-correlation angle between S1_a and S2_a_bottom. The projection of the energies along the large axis of the ellipse is indicated by the blue line. The ellipses in blue, red and green, indicate respectively the 2D-Gaussian fit at 1,2 and 3 σ . The events present "outside" the 3 σ ellipse are cut from the dataset.

Evolution of Calibration quantities over time

In this appendix, the evolution of the calibration quantities over time are shown.

The Light Yield at 32.2 keV is **stable** during the several months studied. The linear fit gives an average value of (7.849 ± 0.002) PE/keV, with a χ^2/NDF of 43.59/7. All data points are consistent with the linear fit at 0.5 %.

The Light Yield at 9.4 keV is **stable** during the several months studied. The linear fit gives an average value of (9.733 ± 0.014) PE/keV, with a χ^2/NDF of 2.694/7. All data points are consistent with the linear fit at 0.5 %.

The linear fit is made on a smaller delay time range (1 000 - 1 500 ns), where the number of event per slices is small. As a consequence, the systematic errors (that come from the slice per slice Gaussian Fit) are over-estimated. This explains why the $\tilde{\chi}^2$ is smaller for the Light Yield at 9.4 keV than the one at 32.2 keV.

The Charge Yield **increases** by $\approx 2.5\%$ between February and April, 2017. The behaviour is due to an increase of the Electron Lifetime on the same period. The correction of the S2 signals by the Electron Lifetime was under estimated, giving a bigger Charge Yield.

As expected, the Electron Lifetime **increases** by $\approx 9\%$ from February to May. This behaviour is induced by improvement on the purification system, and thus, a reduction of the number of impurities in the LXe.

The Energy Resolutions of S1_a, S2_a and of the CES are **stable** during the few months studied. The linear fits give average values indicated in the Table C.1. The $\tilde{\chi}^2$ of the linear fits are also indicated in this Table. They are all smaller or of the order of the unity, indicating that the three distributions are consistent with a linear fit. All data points are consistent with the linear fit at 5 %.

	Resolution at 41.6 keV (%)	χ^2/NDF
CES	5.46 ± 0.03	7.51/7
S1_a	7.67 ± 0.08	2.3/7
S2_a_bottom	13.41 ± 0.11	0.65/7

Table C.1 – Energy Resolution for the calibration campaigns form the February 13th, 2017 to the May 16th, 2017. The errors contains systematic and statistic ones.

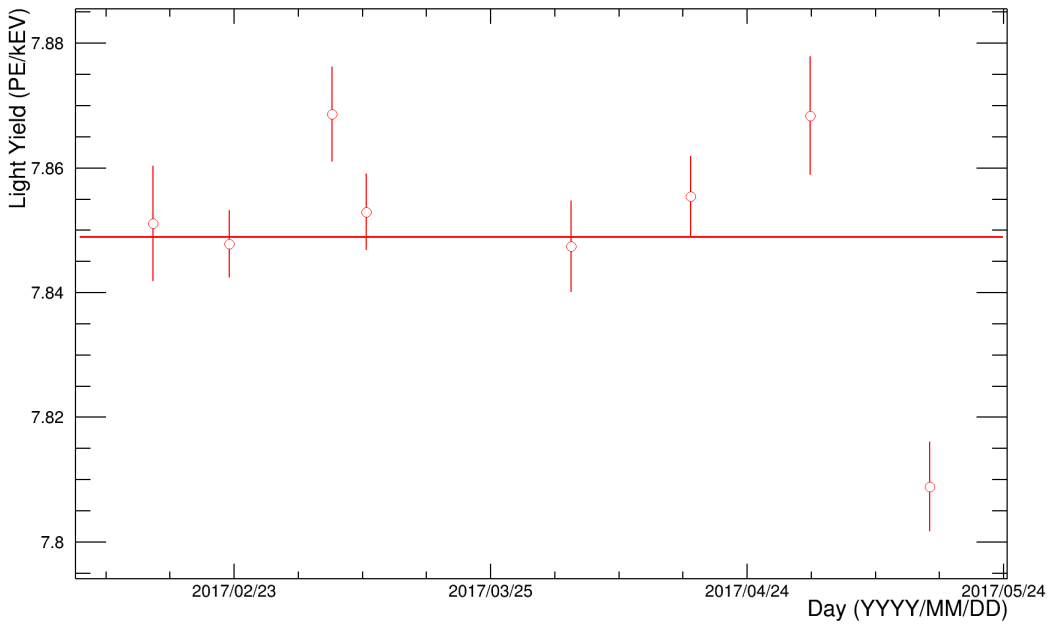


Figure C.1 – Light Yield at 32.2 keV as a function of the time. Each point corresponds at ≈ 24 hours of calibration data recorded. For each calibration campaign, the Light Yield is determined with the method presented in section 3.2.1. The errors bars include the statistic and the systematic errors.

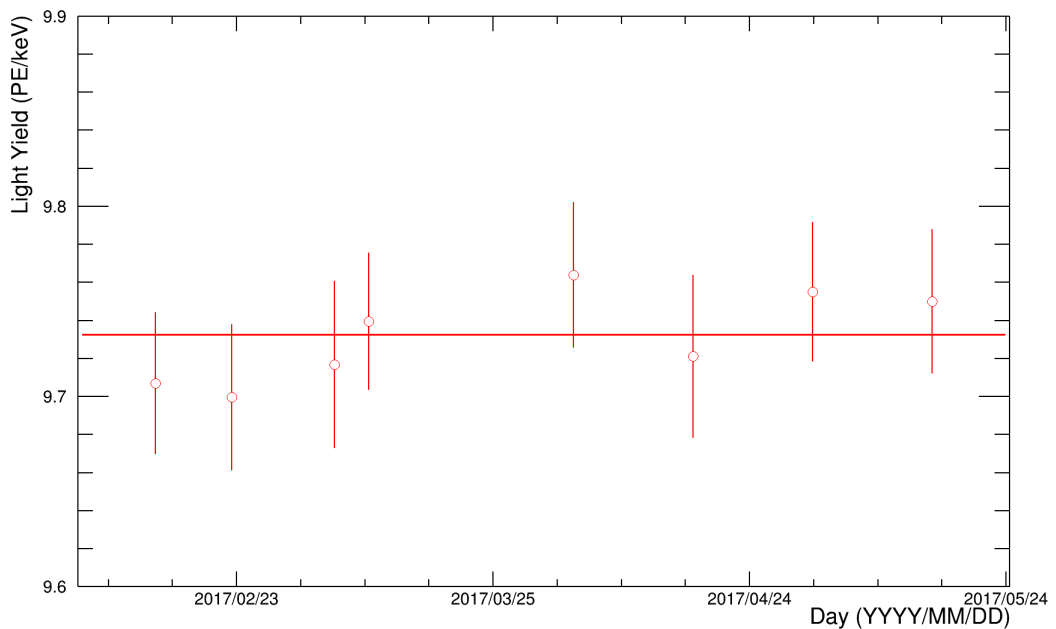


Figure C.2 – Light Yield at 9.4 keV as a function of the time. Each point corresponds at ≈ 24 hours of calibration data recorded. For each calibration campaign, the Light Yield is determined with the method presented in section 3.2.1. The errors bars include the statistic and the systematic errors.

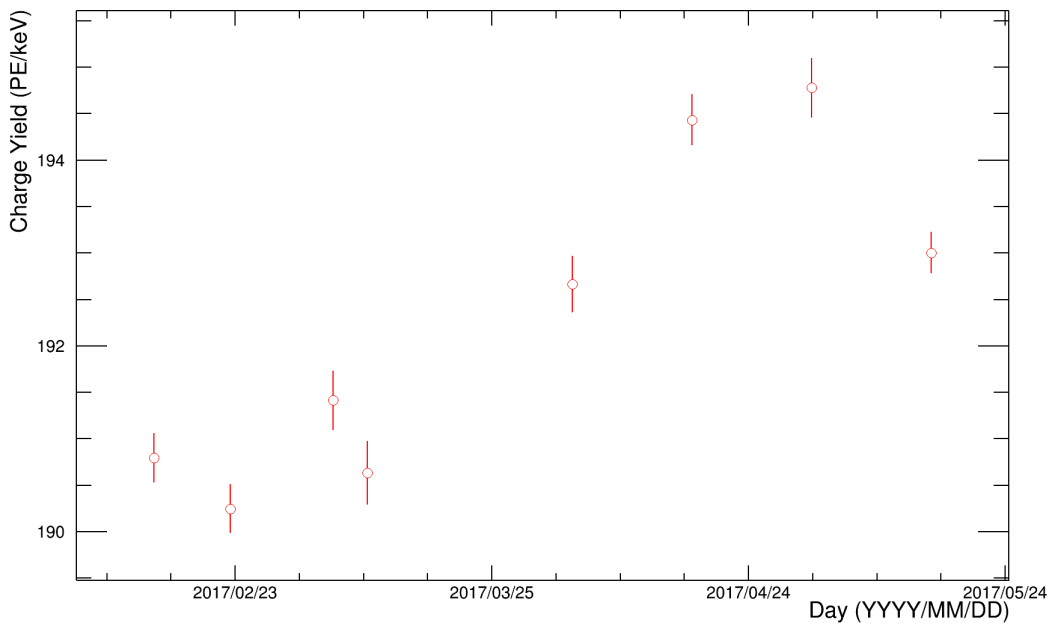


Figure C.3 – Charge Yield at 41.6 keV as a function of the time. Each point corresponds at ≈ 24 hours of calibration data recorded. For each calibration campaign, the Charge Yield is determined with the method presented in section 3.2.2. The errors bars include the statistic and the systematic errors.

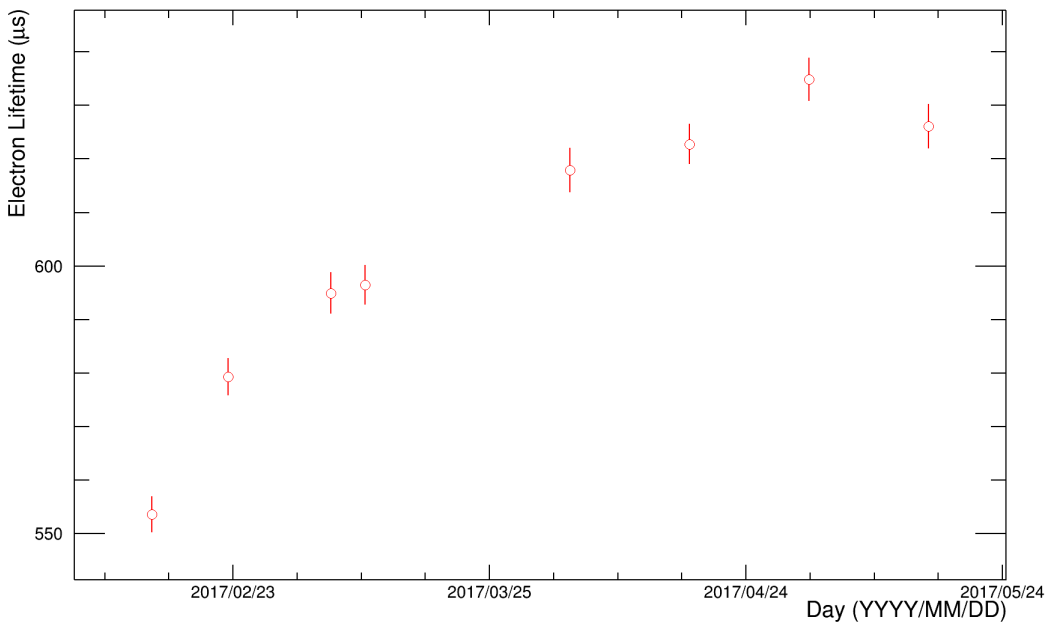


Figure C.4 – Electron Lifetime as a function of the time. Each point corresponds at ≈ 24 hours of calibration data recorded. For each calibration campaign, the Electron Lifetime is determined with the method presented in section 3.2.3. The errors bars include the statistic and the systematic errors.

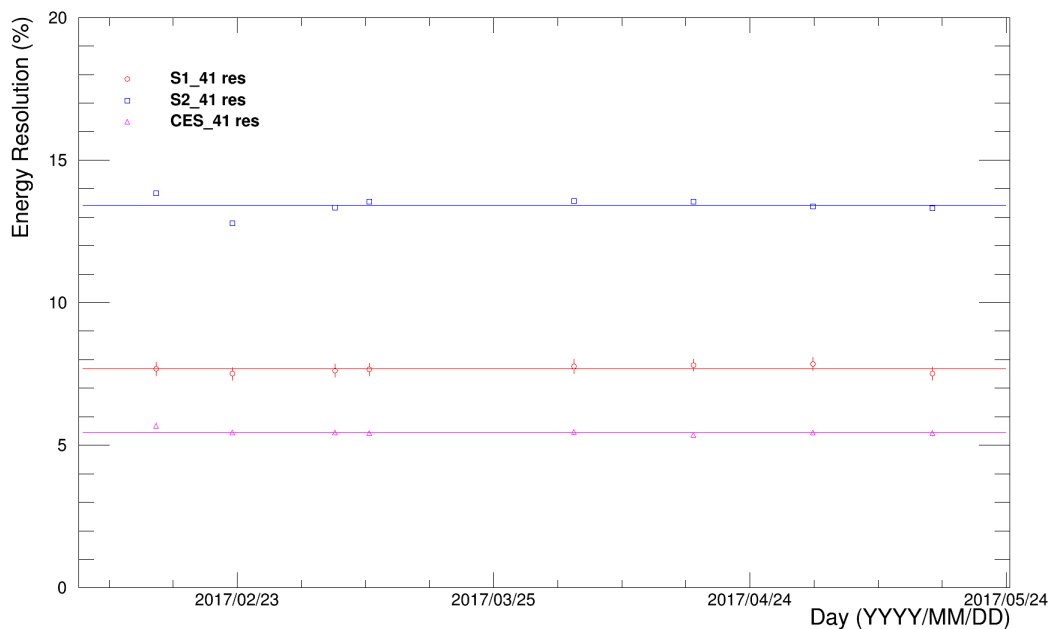


Figure C.5 – Energy Resolution at 41.6 keV as a function of the time. Each point corresponds at ≈ 24 hours of calibration data recorded. For each calibration campaign, the Energy Resolution is determined with the method presented in section 3.2.4. The errors bars (within the points) include the statistic and the systematic errors.

Determination of the Electrons' Velocities at Different Drift Fields

The Z coordinate of the interaction depends on electrons' drift velocities, v_d , in the TPC, which depends itself on the drift field : the bigger the field, the faster electrons drift.

$$Z = v_d \cdot \Delta t \quad (\text{D.1})$$

To determine the electrons' drift velocities at different drift field, we use :

$$v_d = \frac{Z_{max}}{\Delta t_{max}} \quad (\text{D.2})$$

Where Z_{max} is the maximal Z position, and thus equals the height of the TPC : $Z_{max} = 96.9 \text{ cm}$, and where Δt_{max} is the maximal Drift Time.

The Drift Time maximal (determined thanks to Figure D.1) and the corresponding electrons' drift velocities are given for different electric fields in Table D.1.

Field (V/cm)	Drift Time Maximal (μs)	Electrons' Drift Velocity (cm/ μs)
40	955	0.10
50	850	0.11
60	785	0.12
70	747	0.13
80	717	0.14
120	670	0.16

Table D.1 – Determination of the electrons' drift velocities at different drift field.

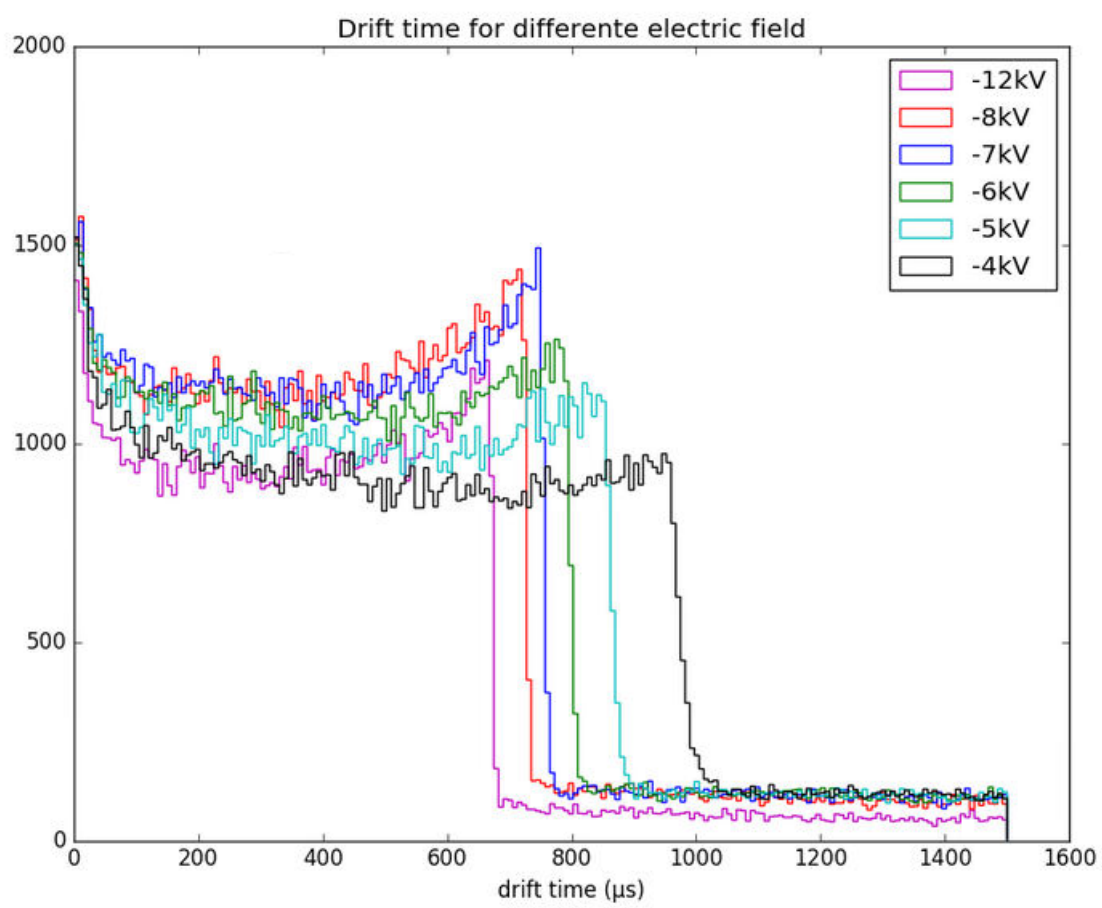


Figure D.1 – Drift Time distribution at different drift field applied in the TPC

Evolution of Calibration quantities with the drift field

In this appendix, the evolution of the calibration quantities with the drift field is shown.

The S1 and S2 signals depend on the number of electrons that escape the recombination with xenon atoms. The stronger the electric field is, the more electrons can escape the recombination, giving a more intense S2 signal, but a less intense S1 signal, and thus a smaller Light Yield.

In the next Figures, we verified that **the Charge Yield increase when the Light Yield decrease**. The Light Yield at 32.2 keV decrease by $\approx 12\%$, the Light Yield at 9.4 keV decrease by $\approx 9\%$, while the Charge Yield increase by $\approx 23\%$ with the drift field.

The Electron Lifetime is stable from 40 and 80 V/cm, with an average value of $(531.72 \pm 2.13) \mu s$ (and with a χ^2 of 3.45/4).

The Electron Lifetime do not depend on the drift field, but only on the number of impurities. The Electron Lifetime decrease at 120 V/cm¹ because the number of impurities decrease from November 2016 to February 2017. In all case, our Electron Lifetime is consistent with one provided by the XENON collaboration.

The Energy Resolutions at 41.6 keV are **stable** with the drift field applied in the TPC. The average values obtained by the linear fits are given in Table E.1.

	Resolution at 41.6 keV (%)	χ^2/NDF
CES	8.2 ± 0.12	7.3/5
S1_a	13.02 ± 0.23	3.8/5
S2_a_bottom	13.44 ± 0.27	2.19/5

Table E.1 – Average value of the Energy Resolutions, for different drift field. The errors contains systematic and statistic ones.

¹The dataset at 120 V/cm was recorded in November 2016.

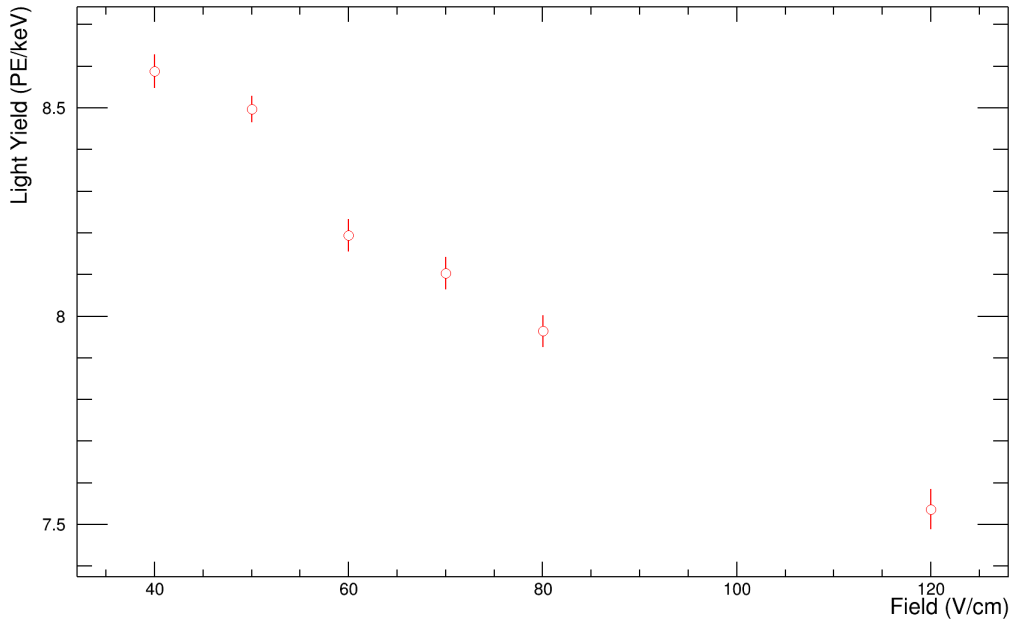


Figure E.1 – Light Yield at 32.2 keV as a function of the drift field applied in the TPC. Each point corresponds at ≈ 2 hours of calibration data recorded. For each point, the Light Yield is determined with the method presented in Chapter 4. The errors bars include the statistic and the systematic errors.

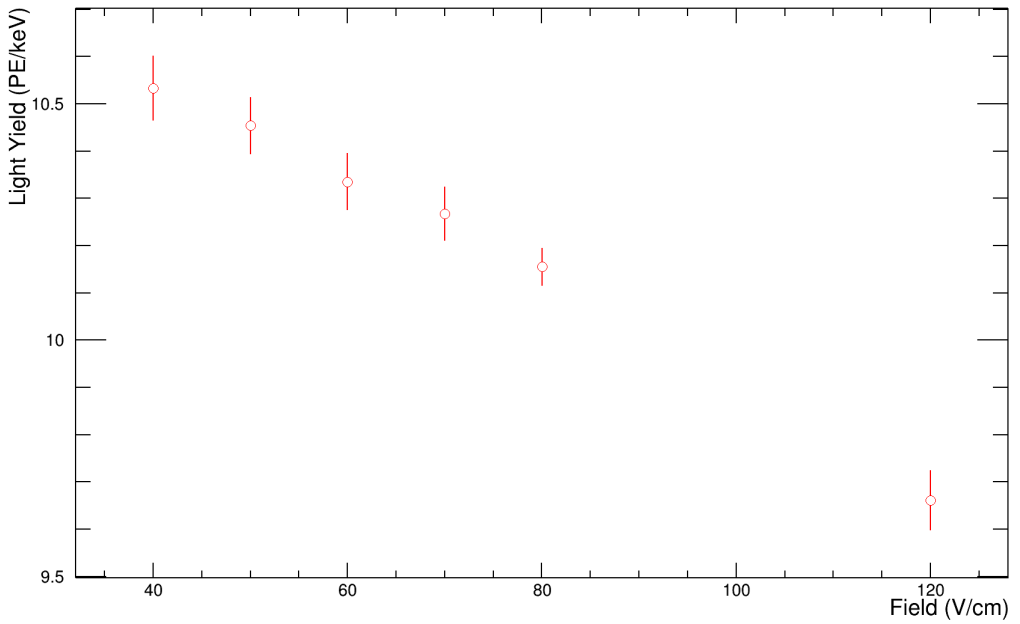


Figure E.2 – Light Yield at 9.4 keV as a function of the drift field applied in the TPC. Each point corresponds at ≈ 2 hours of calibration data recorded. For each point, the Light Yield is determined with the method presented in Chapter 4. The errors bars include the statistic and the systematic errors.

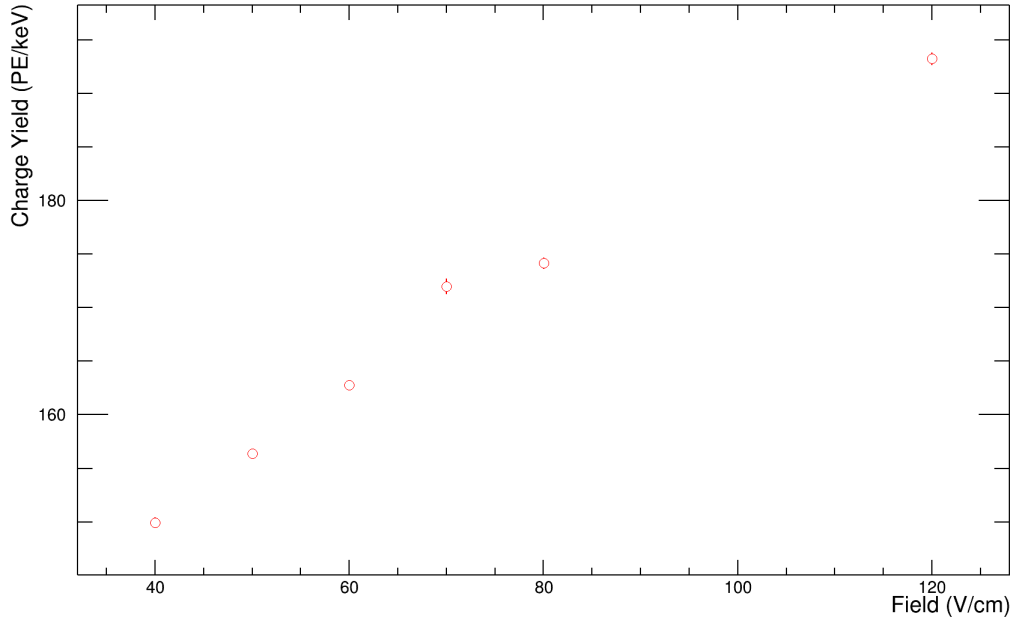


Figure E.3 – Charge Yield at 41.6 keV as a function of the drift field applied in the TPC. Each point corresponds at ≈ 2 hours of calibration data recorded. For each point, the Charge Yield is determined with the method presented in Chapter 4. The errors bars include the statistic and the systematic errors.

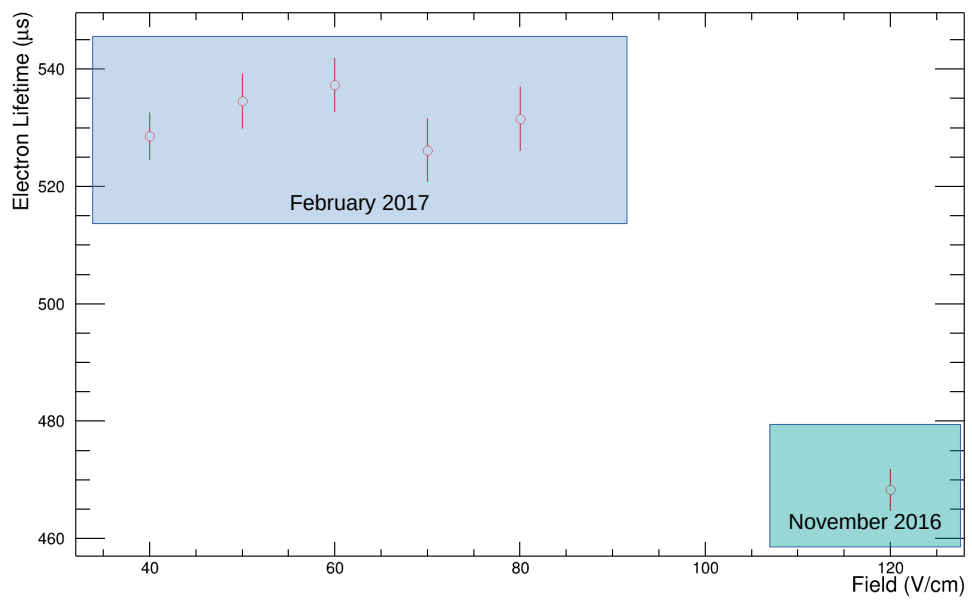


Figure E.4 – Electron Lifetime as a function of the drift field applied in the TPC. Each point corresponds at ≈ 2 hours of calibration data recorded. For each point, the Electron Lifetime is determined with the method presented in Chapter 4. The errors bars include the statistic and the systematic errors. Boxes indicate the date and the expected value from the Electron Lifetime corresponding to the purity at the time of the data-taking.

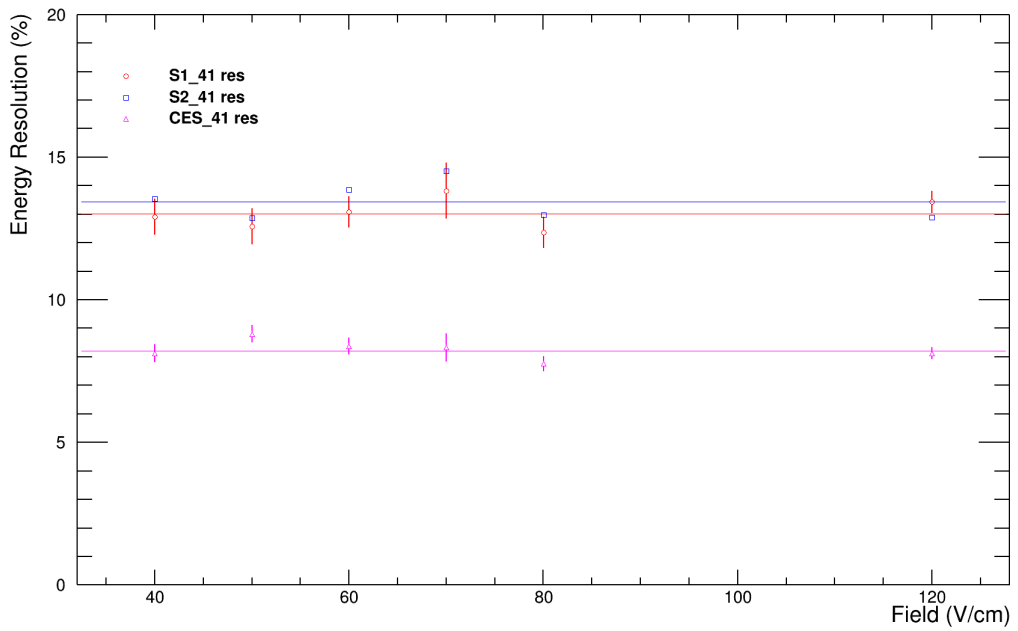


Figure E.5 – Evolution of the Energy Resolution at 41.6 keV as a function of the drift field applied in the TPC. Each point corresponds at ≈ 2 hours of calibration data recorded. For each point, the CES and the Energy Resolution are determined with the method presented in Chapter 4. The errors bars include the statistic and the systematic errors.

Bibliography

- [1] F. Zwicky. On the masses of nebulea and of clusters of nebulea. *Astrophysical Journal, Volume 86, Number 217*, 1937.
- [2] V. Rubin, W. Ford Jr, and N. Thonnard. Rotational properties of 21 sc galaxies with a large range of luminosities and radii, from ngc 4605 (r= 4kpc) to ugc 2885 (r=122 kpc). *Astrophysical Journal, Volume 238, Number 471*, 1980.
- [3] M. Le Calloch. *Study of the single electron charge signals in the XENON100 direct Dark Matter search experiment*. PhD thesis, Université de Nantes, 2014.
- [4] Volker Springel and al. Simulations of the formation, evolution and clustering of galaxies and quasars. *Nature, Volume: 03597, Number: 435*, 2005.
- [5] P.A.R Ade Plank Collaboration and al. Planck 2015 results. xiii. cosmological parameters. *Astrophysical Journal, arXiv: 1502.01589v3*, 2016.
- [6] Gianfranco Bertone and Dan Hooper AND Joseph Silk. Particle dark matter: Evidence, candidates and constraints. *High Energy Physics - Phenomenology, arXiv: 0404175v2*, 2004.
- [7] M. Goodman and E. Witten. Detectability of certain dark-matter candidates. *Physical Review D, Volume 31, Number 12*, 1985.
- [8] J.D. Lewin and P.F Smith. Review of mathematics, numerical factors, and corrections for dark matter experiments based on elastic nuclear recoil. *Astroparticle Physics, Volume 6, Number 87-112*, 1996.
- [9] C. Patrignani and al. Particle data group - dark matter. *Chinese Physics C, Volume 40*, 2016.
- [10] E. Aprile and al. First dark matter search results from the XENON1t experiment. *Cosmology and Nongalactic Astrophysics, arXiv: 1705.06655v1*, 2017.
- [11] E. Aprile and al. Xenon100 dark matter results from a combination of 477 live days. *Cosmology and Nongalactic Astrophysics, arXiv: 1609.06157v3*, 2016.
- [12] E. Aprile and al. Removing krypton from xenon by cryogenic distillation to the ppq level. *Instrumentation and Detectors, arXiv: 1612.04284v1*, 2016.
- [13] D. Cline and al. A wimp detector with two-phase xenon. *Astroparticle physics, 373-377*, 1999.
- [14] F.V Massoli. *The XENON1T experiment: Monte Carlo background estimation and sensitivity curves study*. PhD thesis, Universita di Bologna, 2015.
- [15] Xenon1t Web site. xenon1t.org.
- [16] E. Aprile and al. Observation of anti-correlation between scintillation and ionization for mev gamma-rays in liquid xenon. *Astrophysics, arXiv:0704.1118*, 2007.
- [17] V.E. Guiseppe and al. A radon progeny deposition mode. *Nuclear Experiment, arXiv:1101.0126*, 2011.

- [18] Alessandro Manfredini. Status of the XENON1T experiment. *DBD2016 Workshop, Osaka, Japan.*
- [19] E. Aprile and al. The xenon100 dark matter experiment. *Instrumentation and Methods for Astrophysics*, arXiv: 1107.2155v2, 2012.
- [20] E. Aprile. Liquid xenon detectors for particle physics and astrophysics. *High Energy Physics - Experiment*, arXiv: 0910.4956v1, 2009.
- [21] J. Aalbers, C. Tunnell, and B. Pelssers. PAX: The XENON1T raw data processor. *XENON1T inauguration poster*, 2015.
- [22] Nucl. data sheets. *NuDat*, 2015.
- [23] K. J. Ma and al. Time and amplitude of afterpulse measured with a large size photomultiplier tube. *Instrumentation and Detectors*, arXiv:0911.5336v1, 2009.
- [24] E. Aprile and al. Physics reach of the xenon1t dark matter experiment. *Instrumentation and Detectors*, arXiv:1512.07501, 2016.
- [25] L. W. Kastens and al. Calibration of a liquid xenon detector with kr83m. *Physical Review C* 80:045809, 2009.
- [26] A. Manalaysay and al. Spatially uniform calibration of a liquid xenon detector at low energies using kr83m. *Review of Scientific Instruments* 81:073303, 2010.
- [27] E. Aprile and al. Measurement of the scintillation yield of low-energy electrons in liquid xenon. *Physical Review C* 86:112004, 2012.
- [28] L. Baudis and al. Response of liquid xenon to compton electrons down to 1.5 kev. *Physical Review D* 87:115015, 2013.
- [29] J. Thomas and D.A. Imel. Recombination of electron-ion pairs in liquid argon and liquid xenon. *Physical Review A*, Volume 36, Number 15, 1987.

Calibration of the XENON1T experiment at low energy using a Kr83m Source

Abstract

In the last century, several astrophysical observations have provided strong evidences of the existence of Dark Matter in the Universe. This Dark Matter, non-luminous, and weakly interactive with ordinary matter, could be composed of massive particles, called WIMPs. XENON1T, the third direct detection experiment of the XENON collaboration, uses a dual-phase (liquid-gas) time projection chamber, filled with xenon to detect an elastic scattering of a WIMP with xenon nuclei. The energy transfer during such interaction induces a nuclear recoil with a low energy (under 100 keV). It is essential to calibrate the detector in the energy range where Dark Matter is expected. Therefore, the XENON collaboration carries out several calibration campaigns with a ^{83m}Kr source, which emits two γ -rays at low energies (32.2 keV and 9.4 keV), allowing the studies of the detector response and its stability. Since the search for Dark Matter requires the use of the detector during several years, it is essential to know its characteristics throughout the experiment, but it is also important to have a detector as stable as possible.

In this report, the calibration at low-energy and the study of the XENON1T stability using a ^{83m}Kr source are presented. The light and charge yield, the electron lifetime, and the detector energy resolution are determined for three months of calibration campaigns. An additional study of the detector behaviour at different electrical fields is also presented and will be thoroughly investigated during the rest of my internship in the Xenon group.

Résumé

Depuis la fin du dernier siècle, de nombreuses observations astrophysiques ont apporté des preuves de l'existence de la Matière Noire dans l'Univers. Cette Matière Noire, non-lumineuse, et interagissant faiblement avec la matière ordinaire, pourrait être composée de particules massives, appelées WIMP. XENON1T, la troisième expérience de détection directe de Matière Noire de la collaboration XENON, utilise une chambre à projection temporelle à double-phase (liquide-gaz) remplie de xénon afin de détecter la diffusion élastique induite par un WIMP sur un noyau de xenon. Le transfert d'énergie provenant de cette interaction provoque un recul nucléaire de faible énergie (inférieur à 100 keV). Avant de pouvoir détecter la Matière Noire, il est indispensable de calibrer le détecteur dans la gamme d'énergie où elle est attendue. Pour cela, la collaboration XENON a mené plusieurs campagnes de calibrations utilisant une source de ^{83m}Kr , qui décroît en émettant deux rayonnements γ à basse énergies (32.2 keV et 9.4 keV). Ces rayonnements permettent de déterminer la réponse du détecteur XENON1T ainsi que sa stabilité de XENON1T. Puisque la recherche de la Matière Noire nécessite d'utiliser le détecteur pendant plusieurs années, il est indispensable de connaître ses caractéristiques durant toute la durée de l'expérience, mais il est aussi important que le détecteur soit aussi stable que possible.

Dans ce rapport, la calibration et l'étude de la stabilité du détecteur XENON1T à basse énergie, utilisant une source de ^{83m}Kr , sont présentées. Le rendement de lumière et de charge, le temps de vie des électrons dans la chambre, ainsi que la résolution en énergie du détecteur, sont déterminés pour trois mois de campagnes de calibrations. Une étude supplémentaire du comportement du détecteur pour différents champs électriques est également présentée et sera étudiée plus en profondeur pendant le reste de mon stage dans le groupe Xénon.